JOURNAL OF PETROLOGY | VOLUME 49 | NUMBER 6 | PAGES 1133–1160 | 2008 | doi:10.1093/petrology/egn020

Fluid and Halide Melt Inclusions of Magmatic Origin in the Ultramafic and Lower Banded Series, Stillwater Complex, Montana, USA

J. J. HANLEY[1]*, J. E. MUNGALL[2], T. PETTKE[3], E. T. C. SPOONER[2] AND C. J. BRAY[2]

[1]DEPARTMENT OF GEOLOGY, SAINT MARY'S UNIVERSITY, 923 ROBIE STREET, HALIFAX, NOVA SCOTIA, CANADA, B3H 3C3

[2]DEPARTMENT OF GEOLOGY, UNIVERSITY OF TORONTO, 22 RUSSELL STREET, TORONTO, ONTARIO, CANADA, M5S 3B1

[3]INSTITUTE OF GEOLOGICAL SCIENCES, UNIVERSITY OF BERN, BALTZERSTRASSE 1–3, CH-3012 BERN, SWITZERLAND

RECEIVED JULY 23, 2006; ACCEPTED MARCH 27, 2008

Fluid and melt inclusions trapped in igneous rocks below the platinum-group element (PGE)-rich J-M reef in the Stillwater Complex, Montana provide a physiochemical record of a continuum of high P–T *magmatic–hydrothermal and low* P–T *metamorphic events. Magmatic–hydrothermal volatiles ranged from NaCl-dominated halide melts (>82 wt % $NaCl_{equiv}$) to more complex Na–Ca–K–Fe–Mn–Ba–Si–Al–Cl brines (28–79 wt % $NaCl_{equiv}$) that were trapped simultaneously with a moderate density carbonic fluid ($CO_2 \pm CH_4$). Early primary inclusions containing immiscible brine and carbonic fluid were trapped in the granophyric albite–quartz core of a zoned pegmatite body in the Gabbronorite* I *unit at* T *of ~ 700–715°C, and* P *between 4·3 and 5·6 kbar. The pegmatitic body crystallized from a fluid-saturated residual silicate liquid that was channeled through the cooling igneous stratigraphy. Approximately 500 m stratigraphically below the pegmatite, in the Ultramafic Series, early halide melt inclusions representing samples of formerly molten NaCl were trapped in unaltered primary olivine over a minimum range in temperature of 660–800°C. In the same olivine that hosts the halide melt inclusions, secondary brine inclusions with a composition similar to brines in the pegmatite were trapped over a minimum temperature range of 480–640°C. As hydrothermal activity continued during post-solidus cooling of the intrusion, quartz precipitation in the vuggy core of the pegmatite body trapped post-magmatic, immiscible brine and carbonic fluid inclusion assemblages that record a progressive decrease in fluid salinity,* T *and confining* P *from lithostatic to near-hydrostatic conditions. Late secondary inclusions containing regional metamorphic fluids were trapped in quartz in the pegmatite after cooling to zeolite-facies conditions. The late metamorphic fluids were low to moderate salinity, $CaCl_2$–$MgCl_2$–H_2O solutions. Hydrous salt melts, magmatic brines, and non aqueous (carbonic) fluids may have coexisted and interacted throughout much of the late crystallization and post-magmatic history of the Stillwater Complex. Hence, the potential for interaction between exsolved magmatic volatiles and grain boundary-hosted sulfide minerals below the J-M reef at near-solidus temperatures, and the post-magmatic modification of the J-M reef PGE ore compositions by hydrothermal fluids are strongly indicated.*

KEY WORDS: *layered intrusion; volatiles; fluid inclusions; Stillwater Complex; pegmatite*

INTRODUCTION

A variety of mineralogical, textural and geochemical evidence shows that igneous rocks in giant layered intrusions containing platinum-group element (PGE) deposits such as the Bushveld Complex, South Africa, the Stillwater Complex, USA, and the Skaergaard Intrusion, East Greenland were recrystallized and chemically modified by magmatic

*Corresponding author. E-mail: jacob.hanley@smu.ca

Table 1: Summary of published fluid inclusion data for mafic–ultramafic intrusions

Principal references	Intrusion	Key observations
Ballhaus & Stumpfl (1986)	Bushveld, South Africa	Secondary inclusions in postcumulus quartz within the 'normal' (unpotholed) Merensky Reef
Schiffries (1990)		Compositions: NaCl–H_2O (70 to >80 wt % $NaCl_{equiv}$); immiscible NaCl–H_2O–CO_2 (15–60 wt % $NaCl_{equiv}$); hydrated $CaCl_2$ Trapping conditions: $T_t < 750^\circ C$; $P_t = 4$–5 kbar
Larsen *et al*. (1992)	Skaergaard, Greenland	Primary inclusions in quartz, apatite and feldspar hosted in gabbroic pegmatites and intercumulus minerals
Sonnenthal (1992)		Compositions: H_2O–NaCl–CH_4 (<6 mol % CH_4; 17·5–22·8 wt % $NaCl_{equiv}$) Trapping conditions: $T_t = 655$–$770^\circ C$; $P_t = 2{\cdot}9$–$3{\cdot}9$ kbar; fO_2 = FMQ–1·5 to FMQ–2
Ripley (2005)	Duluth, USA	Primary and secondary fluid inclusions occurring in microfractures in contact aureole units Compositions: H_2O–NaCl (high salinity) Trapping conditions: $T_t \sim 500^\circ C$
Frost & Touret (1989)	Laramie, USA	Primary and secondary inclusions in quartz from the Sybille Monzosyenite within the Laramie Anorthosite Complex Compositions: CO_2–CH_4, H_2O–NaCl, and silicate–oxide–chloride–carbonate melt inclusions Trapping conditions for primary CO_2 and melt inclusions: $T_t \sim 950$–$1000^\circ C$; $P_t = 3$ kbar
Glebovitsky *et al*. (2001)	Lukkulaisvaara, Russia	Secondary fluid inclusions in quartz from gabbroic pegmatites, quartz veins and sulfide-bearing alteration assemblages Compositions: H_2O, CO_2, H_2O–NaCl (~43 wt % $NaCl_{equiv}$), CO_2–H_2O, CH_4–N_2, CO_2–CH_4–N_2 Trapping conditions: $T_t = 290$–$370^\circ C$; $P_t = 1{\cdot}4$–$2{\cdot}5$ kbar

volatile phases (Stumpfl, 1974; Schiffries, 1982; Stumpfl & Rucklidge, 1982; Volborth & Housley, 1984; Ballhaus & Stumpfl, 1986; Boudreau & McCallum, 1986, 1992; Boudreau *et al.*, 1986, 1997; Schiffries & Skinner, 1987; Boudreau, 1988, 1992, 1999; Sonnenthal, 1992; Meurer *et al.*, 1999; Willmore *et al.*, 2000; McBirney, 2002). Although the ore metal distribution in some layered intrusions can be explained by mainly magmatic processes (e.g. Campbell *et al.*, 1983; Mungall, 2002), an increasing number of features have been recognized that are in conflict with a purely magmatic model and suggest that fluids played an important role in concentrating the PGE. These include: (1) high PGE grades in ores associated with silicate rocks that formed in association with magma that lacked a sufficiently high PGE content (e.g. Bushveld Critical Zone; Willmore *et al.*, 2000); (2) zones where PGE grades are not well correlated with sulfide content but are well correlated with hydrothermal alteration intensity (e.g. Stillwater, USA, Polovina *et al.*, 2004; Platreef, South Africa, P. Armitage, personal communication); (3) occurrences of PGE-rich rock types such as pegmatites that crosscut or disrupt igneous layering (Boudreau, 1999); (4) a lack of evidence that ore-forming magmas were saturated in PGE-rich sulfide liquid (Cawthorn, 1999); (5) PGE metal ratios (i.e. Pd/Pt) and distributions within ore horizons that cannot be explained entirely by silicate–sulfide melt fractionation (Willmore *et al.*, 2000). In the Stillwater Complex there is a variety of evidence for late-stage hydrothermal reworking of the PGE-rich J-M reef, and earlier, high-temperature volatile activity.

Despite the evidence summarized above, the exact source and composition of the volatiles, and the relative timing of volatile activity relative to other igneous and ore-forming processes are poorly constrained. Consequently, the relative importance of fluids in generating the primary economic grades of the J-M reef or modifying primary ore compositions cannot be accurately evaluated.

The thermochemical information preserved by fluid inclusion assemblages has the potential to address the issues raised above. Nonetheless, to date, there are no fluid inclusion data for the Stillwater Complex and very limited data for other PGE-bearing mafic–ultramafic layered intrusions in general (Table 1). In this study, we characterize the textural and microthermometric characteristics, and discuss the origin, of fluid inclusions and inclusions of molten salt occurring in olivine from a sample of orthopyroxenite in the Bronzitite Zone of the Ultramafic Series, and quartz from the core of a pegmatite in Gabbronorite I Zone of the Lower Banded Series. The samples studied occur stratigraphically below the PGE-rich J-M reef.

GEOLOGICAL SETTING AND BACKGROUND

The Stillwater Complex is a late Archean (2701 ±8 Ma crystallization age; DePaolo & Wasserburg, 1979), layered, ultramafic–mafic intrusion occurring along the northern margin of the Beartooth Mountain Range in southwestern Montana, USA (Fig. 1a). The intrusion contains the J-M reef, a stratiform ore horizon that produced ~450 000 oz of Pd and 130 000 oz of Pt in 2005 (Johnson Matthey® 2005 figures). The intrusion is in fault and intrusive contact with a basement of Precambrian metasediments and a quartz monzonite stock that is slightly younger than the Stillwater Complex (by 60 Myr; Nunes & Tilton, 1971). At the lower contact of the complex, metasediments show a hypersthene–cordierite hornfels grade (maximum $T = 825^{\circ}C$, $P = 3$–4 kbar; Labotka & Kath, 2001), consistent with an estimated maximum emplacement depth of 9–12 km. Lower greenschist-facies regional metamorphism at 1·7 Ga (Nunes & Tilton, 1971; Page, 1977) was followed by at least two major episodes of faulting and tilting of the complex.

The Stillwater Complex comprises an ~6 km thick sequence of mafic–ultramafic igneous rocks. Rock units have been subdivided into three major groups consisting of 14–18 zones, defined primarily by their primary mineralogy (Fig. 1b): (1) the Basal series (500 m), composed of a lower norite and upper orthopyroxenite (bronzitite) zone; (2) the Ultramafic Series (1400 m), composed of an upper orthopyroxenite (bronzitite) zone and a lower peridotite zone that hosts the principal chromitite layers; (3) the Banded Series (4500 m), composed of interlayered norites, gabbronorites, troctolites and anorthosites, and hosting the PGE-producing J-M reef near its base (500 m above the upper contact of the Ultramafic Series).

The J-M reef, hosting the principal PGE concentration (average 18·8 ppm Pd + Pt over an average thickness of 2 m; Pd:Pt = 3·4:1; Zientek *et al.*, 2002), occurs within Olivine-Bearing Zone I (OBI; Fig. 1b). Although traceable across the entire complex, the J-M reef is not restricted to a single position within the OBI, nor is it present continuously along strike of the OBI. PGE mineralization in the OBI is associated with an ~1·5 m thick pegmatitic peridotite overlain by troctolite and anorthosite. Locally, mineralized intervals up to 15 m thick define 'ball-room' structures, although the actual thickness of the J-M reef stratigraphic package does not change within these structures (Zientek *et al.*, 2002). The ore mineral assemblage contains 0·5–3·0 vol. % base metal sulfides comprising pyrrhotite, pentlandite and chalcopyrite. With the exception of Pd, the PGE are present as a variety of discrete PGE minerals and alloys that are hosted within aggregates of base metal sulfides, or as inclusions in hydroxysilicate and chromite grains. The majority of the Pd is dissolved in pentlandite where it accounts for ~80% of the total Pd grade (Heyse, 1983).

PREVIOUS WORK ON VOLATILES IN THE STILLWATER COMPLEX

Field, textural and limited geochemical studies (Page, 1976, 1977; McCallum *et al.*, 1980; Volborth & Housley, 1984; Mathez *et al.* 1989; Marcantonio *et al.*, 1993; Czamanske & Loferski, 1996; McCallum *et al.*, 1999; Lechler *et al.*, 2002; Polovina *et al.*, 2004) show that a low-T fluid of presumed metamorphic origin recrystallized primary ore mineral assemblages, down-graded ore tenor, altered host rock compositions, and modified O, Pb and Re–Os isotopic compositions within the Stillwater Complex. Although fracture-controlled (McCallum *et al.*, 1980, 1999; Polovina *et al.*, 2004) and semi-pervasive (Page, 1977; Czamanske & Loferski, 1996) alteration of primary igneous minerals to secondary Ca-Mg-hydroxysilicate rich assemblages is widespread, there is a strong spatial relationship between hydrothermal alteration and the J-M reef over much of its ~35 km strike length (Volborth *et al.*, 1986; E. Mathez, personal communication). Commonly, igneous rocks immediately above and below intensely altered sections of the J-M reef are fresh and unaltered (Heyse, 1983; this study). Although no fluid inclusion studies have been carried out to confirm the conditions of alteration, the hydrothermal activity responsible for the features listed above has been attributed to lower greenschist-facies metamorphism involving <400°C, non-magmatic water at ~1700–1600 Ma (Nunes & Tilton, 1971; Page, 1976, 1977; McCallum *et al.*, 1999; Lechler *et al.*, 2002).

Evidence for earlier, higher temperature, magmatic to post-magmatic volatiles related to the cooling of the intrusion is also widespread. Bulk geochemical data, textural observations, variations in the halogen composition of apatite and phlogopite, and numerical models indicate that a Cl-rich volatile phase chemically modified and recrystallized the igneous rocks in the Stillwater Complex (Boudreau & McCallum, 1986; Boudreau *et al.*, 1986; Boudreau, 1999; Meurer *et al.*, 1999). Thermochemical modeling by Mathez *et al.* (1989) in the C–O–H–Cl system suggested that the volatile phase was initially a water-poor, graphite-saturated CO_2–CO–HCl mixture that evolved down-temperature from supersolidus conditions (>1000°C) to a more water-rich composition. Recent experimental work by Mathez & Webster (2005) showed that the volatile phase must have been very Cl-rich during the latest stages of crystallization of the Stillwater Complex to produce the Cl-rich apatite compositions observed within and below the J-M reef.

Of particular relevance to this study are pegmatite bodies that are abundant in the lower part of the intrusion (Fig. 1b). They occur as irregular bodies, veins, dykes and breccias in the Basal Zone and Ultramafic Series, in the Norite I and Gabbronorite I zones of the Lower Banded Series, and in the Olivine-Bearing I zone (Volborth & Housley, 1984; Braun *et al.*, 1994; Boudreau, 1999). Above the J-M reef, pegmatite bodies are less abundant. The pegmatites formed

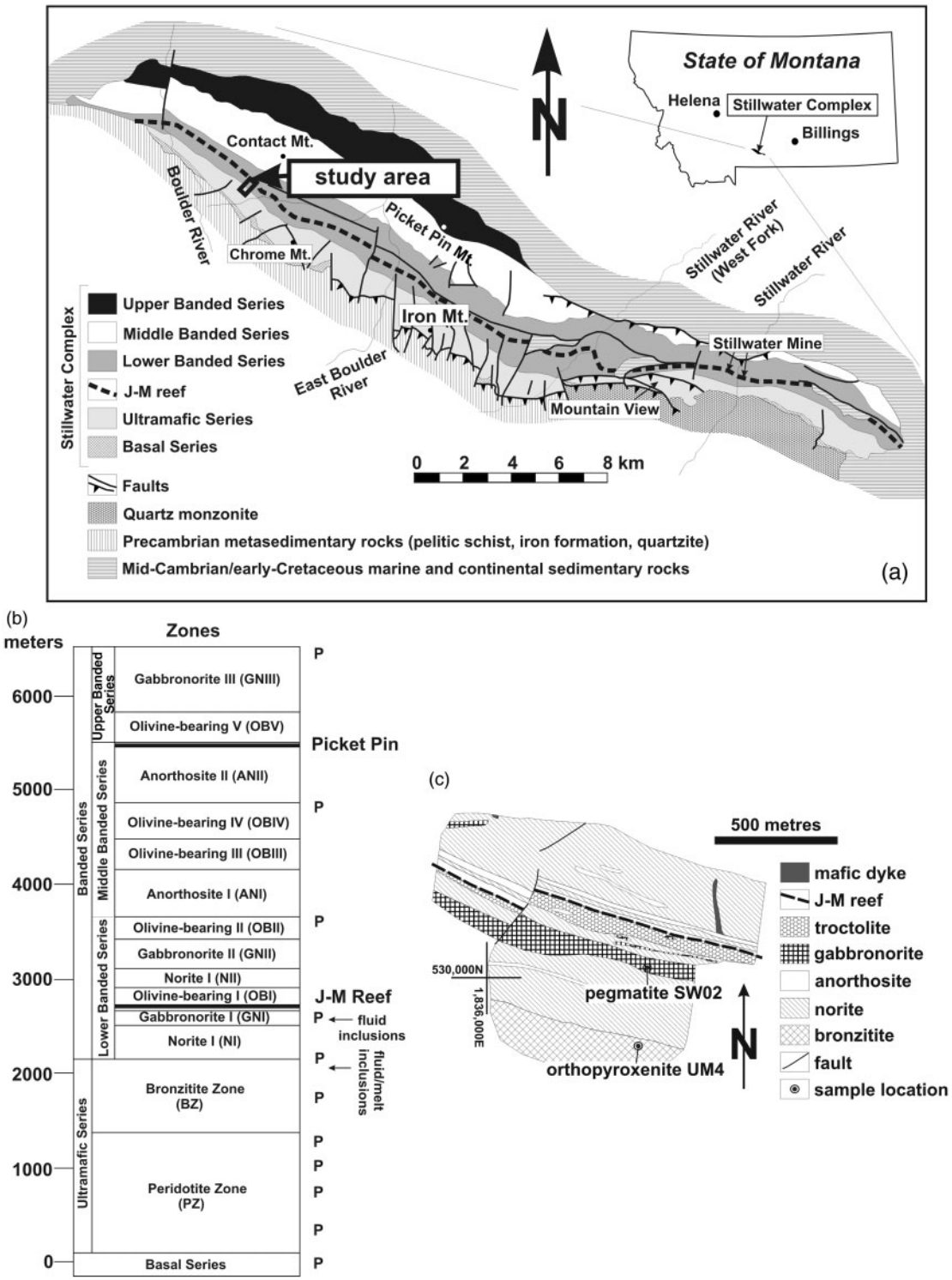

Fig. 1. Geological setting of the study area and sample locations. (a) Generalized plan-view geology of the Stillwater Intrusion showing the study area SW of Contact Mountain. (b) Stratigraphic column for the Stillwater Complex showing the major lithological groups and zones of the igneous sequence, location of pegmatite bodies (P) and the location of the J-M reef and disseminated sulfide mineralization at Picket Pin. The section of the stratigraphy studied is indicated with arrows. (c) Surface map of the sample area showing the location of pegmatite SW02 at the base of Gabbronorite I and orthopyroxenite UM4 from the top of the Bronzitite Zone of the Ultramafic Series. Map units modified from Page & Nokleberg (1974). Coordinates are for the Montana State Plane South system, NAD1927.

as fluids were channeled into distinct pathways as the permeability in the surrounding rocks decreased with increasing progression towards crystallization (Braun *et al.*, 1994; Boudreau, 1999). In these localized pathways, fluid: rock ratios were high. With the exception of extreme coarsening of grain sizes up to 20 cm, and subtle decreases in the Mg-number of pyroxene and An content of plagioclase, the pegmatites are mineralogically identical to their host igneous units (Braun *et al.*, 1994). The chemical composition of the pegmatites shows that volatiles involved in their formation were in equilibrium with a slightly more evolved rock or melt composition (Braun *et al.*, 1994). Locally, the cores of pegmatites hosted in barren stratigraphy below the J-M reef may contain extremely PGE-rich sulfide–arsenide mineralization (Volborth & Housley, 1984; Boudreau, 1999; A. Boudreau, personal communication, 2004). Numerical simulations by Boudreau & Meurer (1999) show that a magmatic volatile phase, exsolved from the crystallizing igneous pile, may have scavenged trace amounts of PGE, Au, S and base metals occurring within the lower part of the igneous stratigraphy. Boudreau & Meurer (1999) have argued that ore metals were transported by volatiles upwards towards the base of the magma chamber. Where the fluid redissolved into fluid-undersaturated silicate melt, PGE-rich sulfides were precipitated to form the stratiform J-M reef deposit.

METHODS

Sampling

Fluid and melt inclusions were observed in two settings: (1) in massive and graphic-textured quartz contained within the felsic cores of coarse-grained gabbroic and gabbronoritic pegmatites hosted within the Gabbronorite I (GNI) Zone of the Lower Banded Series; (2) in olivine grains from orthopyroxenites in the Bronzitite Zone of the Ultramafic Series. After preliminary investigations of several dozen fluid inclusion thin sections from samples in the Contact Mountain, Mountain View, and Chrome Mountain areas (Fig. 1a), two samples were selected as being representative of the preserved inclusion record below the J-M reef and were studied in detail. One sample is a pegmatite (sample SW02) from an exposure of the Lower Banded Series in the Contact Mountain section, at the base of the GNI Zone near the contact with the underlying Norite I zone (Fig. 1b and c). The sample location is stratigraphically 150 m below the J-M reef. The second sample is composed of orthopyroxenite from the Bronzitite Zone of the Ultramafic series (sample UM4), sampled 500 m below the J-M reef, on the same outcrop as the pegmatite SW02.

Mineral chemistry

Mineral analyses were performed using a Cameca SX-50 electron microprobe (EMP) at the University of Toronto. The instrument was operated at 20 kV accelerating voltage with a 10 nA beam current. For all minerals other than feldspar, a beam diameter of 1 μm was used with on-peak counting times of 20 s for all elements. For feldspar, a 5 μm rastered beam was used to minimize Na migration. A variety of synthetic and natural oxides, silicates and halides were used for calibration of the following X-ray lines: Si $K\alpha$ (bustamite, or olivine Fo_{85}), Ti $K\alpha$ (rutile), Al $K\alpha$ (corundum), Fe $K\alpha$ (hematite, or olivine Fo_{85}), Mn $K\alpha$ (bustamite), Mg $K\alpha$ (periclase, or olivine Fo_{85}), Ca $K\alpha$ (bustamite), K $K\alpha$ (sanidine glass), Na $K\alpha$ (albite), Ni $K\alpha$ (pentlandite), Cl $K\alpha$ (tugtupite), F $K\alpha$ (fluorite). Raw microprobe data were reduced using the software package Enterprise for Windows© (Advanced Microbeam, Inc.) which uses standard ZAF correction algorithms. Mineral formulae were recalculated manually and were confirmed using the recalculation software package MinPet (Richard, 1995).

Whole-rock analyses

Whole-rock analyses were determined at the Ontario Geoscience Laboratories Sudbury, Canada. Major elements were analyzed by X-ray fluorescence spectrometry (XRF) on fused lithium metaborate–tetraborate glass disks after loss of ignition (LOI) determination. Trace elements were analyzed by inductively couples plasma mass spectrometry (ICP-MS) after closed vessel, four-acid (HF–HCl–HNO_3–$HClO_4$) digestion. Relative analytical uncertainties for all elements are within ±5%, and are better than ±3% for most trace elements.

Analysis of solid phases in fluid inclusions

Solid phases within fluid inclusions were examined by scanning electron microscope (SEM) using a JEOL JSM-840 instrument with secondary electron and backscattered electron analog imaging and solid-state PGT energy-dispersive (EDS) analytical capabilities. Small chips of quartz and olivine containing fluid inclusions were broken open in a vise, mounted, and carbon-coated. The opened inclusions on the exposed fracture surface were examined. Imaging, X-ray mapping and analysis was carried out at an accelerating voltage of 15–25 kV, sample currents of $1{\cdot}0 \times 10^{-9}$ to $6{\cdot}0 \times 10^{-9}$ A, and a working distance of 15–30 mm. Count rates for spectra collection from solid phases were maximized by adjusting the orientation of the sample mount in the SEM sample chamber. Semi-quantitative analyses of solid phases were obtained using a standardless quantitation routine at a spectrum collection time of 40 s. To test the accuracy of this method, analyses of pure halite ($NaCl$) and a variety of synthetic standards were conducted; these analyses yielded concentrations for major elements within ± 2% of the expected concentrations.

Fluid and melt inclusion microthermometry

Fluid inclusion microthermometry was carried out using a Linkam THMS600 heating–freezing stage mounted on Olympus BX50 and BX51 microscopes, and a Leitz 1350 high-temperature stage (University of Toronto and Saint Mary's University). The Linkam stage was calibrated using the melting temperatures of pure CO_2 (−56·6°C) and pure H_2O (0°C), and the critical T of pure H_2O (374·1°C) using synthetic fluid inclusion standards (R. Bodnar, Bubbles, Inc.). The Leitz stage was calibrated using the melting temperatures of pure silver metal (962°C), lithium fluoride (870°C), sodium chloride (801°C), and barium nitrate (592°C). For quartz-hosted inclusions, the uncertainties associated with microthermometric measurements are ±5°C for $T_{measured} > 560$°C, ±0·2°C for $T_{measured}$ between −190 and 0°C, and ±0·5°C for $T_{measured}$ between 0 and 560°C. A higher heating rate (5°/min on the Linkam stage and 10°/min on the Leitz stage) was used in studying olivine-hosted inclusions to avoid oxidation of the olivine. This resulted in uncertainties of ±2°C for $T_{measured}$ between 0 and 560°C and ±10°C for $T_{measured}$ above 560°C.

RESULTS

Petrology of inclusion-bearing rocks

The pegmatite studied is sub-vertical and roughly perpendicular to the local stratigraphy. It is 60 cm in diameter and about 2 m long. The pegmatite is zoned into three mineralogically distinct parts (Fig. 2a and b): (1) a margin

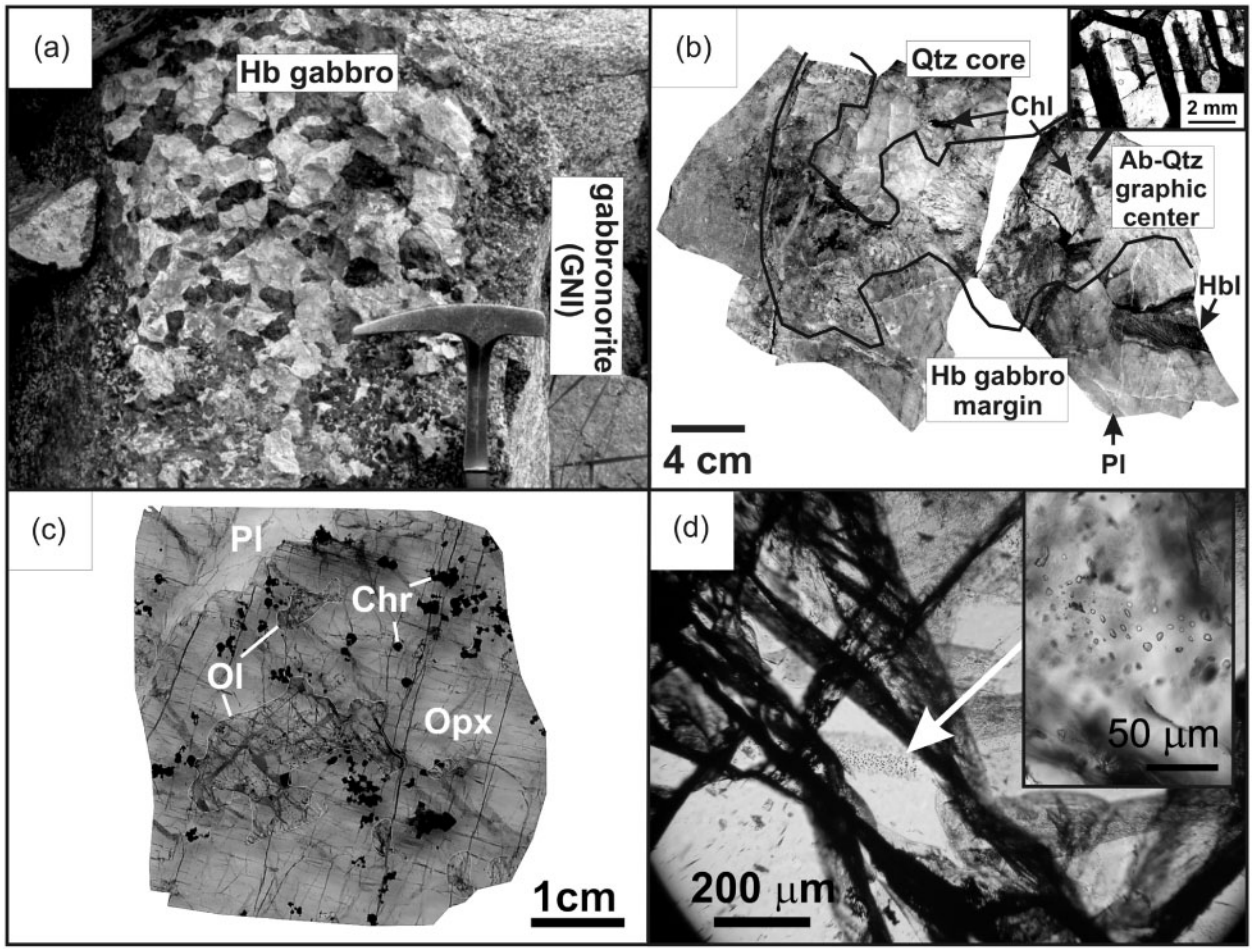

Fig. 2. Field and petrographic characteristics of pegmatites and unaltered orthopyroxenite that host fluid inclusions. (a) Outcrop view of a coarse-grained hornblende gabbro pegmatite body hosted within the gabbronorite (GNI). (b) Polished section (hand sample) through the pegmatite studied (SW02) showing the margin zone of coarse-grained hornblende gabbro (Hb, hornblende; Pl, plagioclase), a center zone of albite–quartz granophyre (graphic texture), and a core zone consisting of massive quartz infilling in a miarolytic cavity. Chlorite (Chl) pseudomorphs after hornblende and clinopyroxene are suspended in the granophyric material at the center of the pegmatite. Inset photomicrograph (plane-polarized light) showing graphic-textured quartz (Qtz)–albite (Ab). (c) Thin section through the orthopyroxenite showing primary phases (Ol, olivine, outlined; Opx, bronzite; Chr, chromite) and interstitial plagioclase (Pl). (d) Photomicrograph (plane light) enlargement of an olivine grain showing a trail of inclusions (arrow). Inset photomicrograph (20°C) shows the trail of inclusions that contain solid halides (see text for description).

zone composed of very coarse-grained (2–10 cm sized crystals) plagioclase + orthopyroxene + clinopyroxene + hornblende that grades diffusely into the surrounding, finer grained but mineralogically similar Gabbronorite I (GNI); (2) a central zone composed of a graphic-textured feldspar and quartz intergrowth containing large, corroded crystals of Mg-chlorite (pseudomorphs after pyroxene and hornblende); (3) a core zone consisting of an infilled miarolitic cavity containing massive quartz. The central and core zones of the pegmatite are volumetrically minor (<10 vol. %) components of the pegmatite body, but they contain quartz that is a robust host phase for fluid inclusion study. We interpret the core zone to be the latest (youngest) stage of the pegmatite, with the central zone representing the petrographic equivalent of the magmatic–hydrothermal transition.

The primary minerals in the orthopyroxenite sample are subhedra of olivine, chromite, orthopyroxene in a matrix of interstitial plagioclase (Fig. 2c). Clinopyroxene oikocrysts are a minor component. The sample contains ~8 vol. % olivine as single, anhedral grains included within large grains of primary orthopyroxene. Phlogopite is a trace interstitial phase (≪0·1 vol. %). The olivine and associated minerals are totally unaltered, but contain secondary fracture networks containing fluid and melt inclusions (Fig. 2d). In contrast to other rocks around the J-M reef that are intensely altered, these fractures are completely free of hydroxysilicate minerals.

Mineral compositions

Pegmatite feldspar composition from SW02 (Table 2) decreases from An_{75} in the margin to end-member albite (Ab_{99}) in the center. Quartz occurs intergrown with plagioclase having a composition always more albitic than Ab_{92}. For comparison, Braun *et al.* (1994) reported plagioclase within quartz-free pegmatites with compositions as high as Ab_{42}. Coarse-grained clinopyroxene in the margin of the pegmatite is augite in composition (Table 2). Hornblende pseudomorphs are magnesiohornblende in composition (Table 2) and contain up to 0·4 wt % F and 0·2 wt % Cl. Chlorite pseudomorphs are ripidolite in composition (Table 2). Olivine, hosting fluid and melt inclusions from sample UM4, has a compositional range of $Fo_{84–85}$ (Table 2) and shows no textural evidence of alteration despite the presence of volatile-bearing inclusions (see below).

Fluid and melt inclusion descriptions

Six fluid and melt inclusion types were observed: type I polyphase brine inclusions; type II carbonic fluid inclusions; type III mixed polyphase brine–carbonic fluid inclusions; type IV halide melt inclusions; type V two-phase aqueous inclusions; type VI silicate melt inclusions.

Type I, polyphase brine inclusions

Type I inclusions contain an aqueous liquid phase (L_{aq}), a small vapour bubble (V_{aq}; <10 vol. %), and multiple solid phases (Fig. 3a–d). They occur in quartz and olivine. In the olivine, type I inclusions occur along healed fracture planes and are secondary in origin. In quartz, type I inclusions occur with type II and type III inclusions in a coeval primary assemblage (see discussion below). Rarely, type I inclusions occur in trails with type II and type III inclusions. These trails are interpreted to be secondary with respect to primary type I inclusions, but are early with respect to other secondary inclusions related to late metamorphism. Type I inclusions are equi-dimensional and commonly show negative crystal shapes in the graphic quartz. In the massive quartz, type I inclusions are elongate, tube-shaped, or rarely 'thorn'-shaped in appearance.

Up to 16 solid phases were observed in the type I inclusions; the composition of 12 of them were determined by SEM-EDS (Table 3). Solid phases are generally more abundant in type I inclusions. Of these, 10 are considered to be true daughter minerals on the basis of their consistent volumetric fill ratios and their presence in the majority of type I inclusions examined. The most unusual daughter mineral is an unnamed Fe–Mg–Ca–Si–Cl–O phase (SX_7); on a Fe–Mn–Si ternary diagram (mol % composition; Fig. 4), the mineral has a variable composition defining a large field lying between magnetite–jacobsite solid solution [Fe_3O_4–$(Mn^{2+},Fe^{2+},Mg)(Fe^{3+},Mn^{3+})_2O_4$], ferropyrosmalite [$(Fe^{2+},Mn)_8Si_6O_{15}(OH,Cl)_{10}$], and pyroxferroite [$(Fe^{2+},Mn)_7(Si_7O_{21})$] end-members. Calcite and rutile are the other two solids identified, but these show variable infill ratios, do not dissolve during heating, and occur as solid inclusions in the host quartz; therefore, they are considered to be only accidentally trapped phases (Fig. 5). The other unidentified solid phases are very rare and are also considered to have been accidentally trapped during inclusion formation.

In olivine, type I inclusions contain halite and up to six additional solids. Halite, and solid phases SX_5 and SX_7 were observed in most type III inclusions in olivine.

Type II, carbonic fluid inclusions

Type II inclusions are mainly single phase at 20°C and contain liquid CO_2 or critical density CO_2 fluid (Fig. 3e), based on their microthermometric behavior (see below). They occur only in quartz and were not observed in any olivine-bearing samples. Type II inclusions occur coevally with type I and type III inclusions (see below). Calcite and rutile are relatively common as accidentally trapped minerals and show highly variable phase ratios. Like type I inclusions, type II inclusions are subrounded or show well-defined negative crystal shapes in the graphic

Table 2: Representative analyses (EMP) of minerals from pegmatite SW02 and orthopyroxenite UM4

Mineral	plagioclase	plagioclase	plagioclase	pyroxene	chlorite	olivine	hornblende
Location	margin SW02[1]	center SW02	center SW02	margin SW02[2]	core SW02[3]	UM4[4]	margin SW02[5]
SiO_2 (wt %)	48·50	62·83	66·38	57·99	25·78	39·86	48·90
TiO_2	–	–	–	0·02	0·05	–	1·00
Al_2O_3	32·52	23·90	19·57	0·69	21·73	–	5·67
FeO	0·46	0·09	0·06	7·71	19·41	14·54	10·18
MnO	0·03	0·23	–	0·22	0·1	0·28	0·16
NiO	–	–	–	–	–	0·30	–
MgO	0·03	0·09	–	20·06	19·5	44·46	16·12
CaO	15·61	4·71	0·19	13·29	0·02	–	12·08
Na_2O	2·85	8·66	11·85	0·09	–	–	0·80
K_2O	0·03	0·04	0·01	0·01	0·02	–	0·57
H_2O	–	–	–	–	13·61	–	4·20
F	–	–	–	–	–	–	0·42
Cl	–	–	–	–	–	–	0·14
Subtotal	–	–	–	–	–	–	95·95
O=F,Cl	–	–	–	–	–	–	0·21
Total	100·07	100·55	98·06	100·17	100·22	99·44	99·94
Si (p.f.u.)	8·89	11·06	11·86	2·11	5·33	1·00	7·15
Al^{IV}	7·02	4·95	4·12	–	2·67	–	0·85
Al^{VI}	–	–	–	0·03	2·62	–	0·13
Ti	–	–	–	–	0·01	–	0·11
Fe^{3+}	0·01	–	–	–	–	–	0·25
Fe^{2+}	0·07	0·01	0·01	0·24	3·36	0·31	1·00
Mn	0·01	0·03	–	0·01	0·02	0·01	0·02
Ni	–	–	–	–	–	0·01	3·51
Mg	0·01	0·02	–	1·09	6·01	1·67	–
Ca	3·07	0·89	0·04	0·52	–	–	1·89
Na	1·01	2·96	4·11	0·01	–	–	0·23
K	0·01	0·01	–	–	0·01	–	0·11
Cations	20·09	19·94	20·13	4·00	20·02	3·00	15·24
Cl	–	–	–	–	–	–	0·04
F	–	–	–	–	–	–	0·19
Composition	An_{75}	An_{23}	An_1	$En_{59}Fs_{13}$	ripidolite	$Fo_{84·5}$	magnesiohbl

[1]Cations calculated on the basis of 32 O.
[2]Cations calculated on the basis of 6 O.
[3]Cations calculated on the basis of 24 (O,OH); H_2O calculated by difference.
[4]Cations calculated on the basis of 4 O.
[5]Cations calculated on the basis of 23 (O,F,Cl) p.f.u. and average of 15eNK, 13eCNK; cation sums reported rather than single site assignments; H_2O calculated by difference.
Dashes indicate elements not analyzed or machine zeros.

quartz but are elongate, tube-shaped or irregular in appearance in the massive quartz.

Type III, mixed polyphase brine–carbonic fluid inclusions

Type III inclusions contain a single-phase CO_2 portion and an aqueous brine portion with solids at 20°C; the inclusions show highly variable volumetric ratios of CO_2 to brine along single growth zones and trails (Fig. 3f and g). Type III inclusions were identified only in the pegmatite. In all type III inclusions observed, the aqueous brine phase surrounds a CO_2 fluid bubble. At much lower brine contents, the brine occurs as a thin film containing

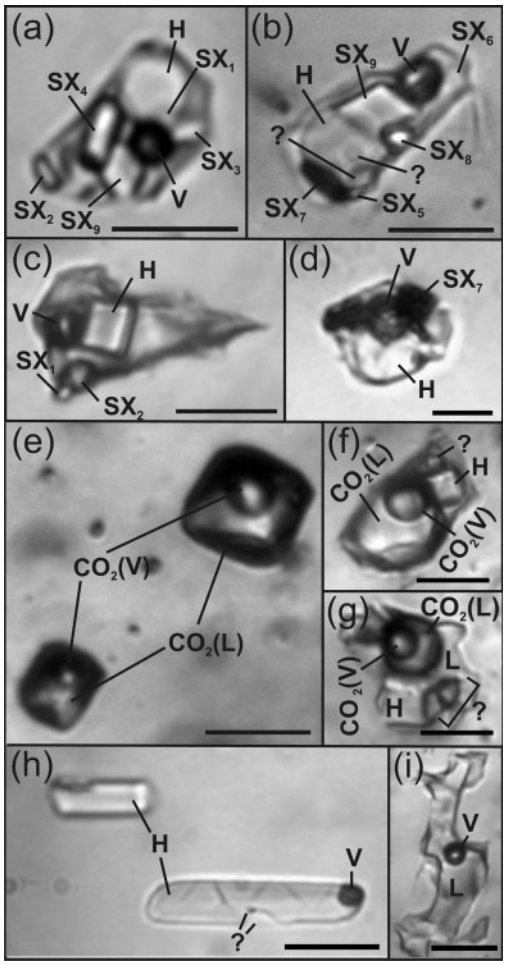

Fig. 3. Photomicrographs (plane-polarized, transmitted light) of inclusion types identified in the pegmatite and orthopyroxenite, taken at 20°C, unless otherwise indicated. Scale bars in all images represent 10 μm. (a–d) Type I brine inclusions hosted in graphic-textured quartz (a and b), massive quartz from the pegmatite core (c), and olivine (d). Phases present: V, vapour; H, halite; SX_1, K-feldspar or muscovite; SX_2, Ca, Cl-bearing phase; SX_3, Ba, Cl-bearing phase; SX_4, lawrencite–molysite; SX_5, 'chalcanthite'; SX_6, sylvite; SX_7, 'pyrosmalite'; SX_8, Fe,Mn,Cl-bearing phase; SX_9, Ca–Fe–Mn carbonate; ?, unknown solid phases. (e) Type II carbonic inclusions in pegmatite quartz. $T = -10$°C. Phases present: CO_2(L), CO_2 liquid; CO_2(V), CO_2 vapour. (f and g) Type III inclusions in pegmatite quartz showing variable volumetric ratios of carbonic fluid and aqueous brine as evidence for heterogeneous coentrapment of immiscible fluids. $T = -10$°C. Phases present: CO_2(L), CO_2 liquid; CO_2(V), CO_2 vapour; L, aqueous brine; H, halite; ?, unidentified solid phases. (h) Type IV inclusions in olivine from orthopyroxenite sample UM4. Phases present: halite (H), a vapour bubble (V) and, in one inclusion, opaque and translucent, unidentified solid phases (?). The lack of any visible aqueous fluid and the non-cubic shape of the inclusions should be noted. (i) Type V late secondary aqueous inclusion in quartz. Phases present: L, aqueous brine; V, vapour.

small solid phases along the walls of the inclusions. The solid phases present are consistent with those observed in the coeval type I inclusions. Like types I and II inclusions, type III commonly contain large, birefringent calcite crystals showing highly variable phase ratios, indicative of accidental trapping. Type III inclusions coexist with type I and type II inclusions in quartz.

Type IV, halide melt inclusions

Type IV inclusions (Fig. 3h) contain a halite crystal filling >90 vol. % of the inclusion volume, 1–2 additional solid phases, a vapour bubble (<10 vol. %) and a thin film of aqueous fluid detected only by cooling the inclusions (Hanley *et al.*, 2005). One solid phase present consistently at constant fill ratios is Ca–Cl-bearing and is interpreted as a true daughter mineral. The inclusions were identified only in olivine and are secondary in origin (Fig. 2d). They have negative crystal shapes or have an elongated, tube-like shape. The halite within the inclusions does not have a cubic morphology but instead mimics the shape of the inclusion wall. This is evidence that the inclusions represent a trapped molten salt phase rather than accidentally trapped halite crystals precipitated from a halite-saturated aqueous fluid (e.g. Erwood *et al.*, 1979; Hanley *et al.*, 2005).

Type V, two-phase aqueous inclusions

Type V inclusions contain an aqueous liquid phase and, rarely, a vapour bubble. They occur in graphic and massive quartz in the pegmatite (Fig. 3i) and are secondary in origin. Rare, early secondary trails of type I, II, and III inclusions are cross-cut and offset by trails of type V inclusions; therefore, type V inclusions must be younger. Type V inclusions are highly irregular in shape and are large relative to other inclusion types (up to ~60 μm in diameter). Where present, the vapour bubble fills ~5 vol. % of the inclusions. No daughter phases were observed.

Type VI, silicate melt inclusions

Rare type VI inclusions occur along growth zones in the graphic quartz, are 5–20 μm in size, and contain a polycrystalline solid (Fig. 6). X-ray mapping and SEM-EDS analysis (Fig. 6) within a type VI inclusion shows that the solids inside are homogeneous in composition and have the following composition (wt %): 6% Fe, 3·5% Mg, 6% Na, 9% Al, 2·5% Ca, 17% Si, 12% Cl, with a balance of ~44% being oxygen and other volatiles not measured. Minor to trace amounts of K, Mn and S were also detected. On the basis of their Si- and Al-rich composition, type VI inclusions are considered to be Cl-rich silicate melt inclusions that recrystallized after entrapment.

Textural characteristics of the brine–CO_2 inclusion assemblages

Photographs and inclusion maps drawn from thin sections (Figs 7 and 8) show representative groups (assemblages) of coexisting type I, II and III inclusions from the pegmatite that were trapped in single, temporally constrained growth features in quartz. The coexistence of these three types of

Table 3: Characteristics of solid phases observed in aqueous and carbonic fluid inclusions

Solid phase	Morphology	Colour	Relief	Birefringence	Origin*	Composition (SEM-EDS)	Species
H	cubic	colourless	high	none	daughter phase	Na, Cl	halite (NaCl)
SX_1	disk; tabular	colourless	moderate	high	daughter phase	K, Al, Si, O	K-feldspar or muscovite
SX_2	needle; prism	green	high	none	daughter phase	Ca, Cl	unnamed Ca-chloride
SX_3	prism	colourless	high	high	daughter phase	68% Ba, 32% Cl	unnamed Ba-chloride
SX_4	prism	yellow	high	low	daughter phase	33–66% Fe, 1–2% Mn, 33–65% Cl	lawrencite, molysite ($FeCl_3$, $FeCl_2$)
SX_5	rounded	purple–pink	moderate	none	daughter phase	Cu, As, S, O	'chalcanthite' ($CuSO_4 \cdot 5H_2O$)
SX_6	tabular	colourless	low	none	daughter phase	K, Cl	sylvite (KCl)
SX_7	hexag. 'barrel'	opaque or red	high	none	daughter phase	27–48% Fe, 2–17% Mn, 0·5–2% Ca, 0·5–2% Ca, 0·5–25% Si, 0·1–8% Cl, O	?? 'pyrosmalite-like'
SX_8	rounded disk	yellow–brown	moderate	high	daughter phase	80% Fe, 0·4% Mn, 19·6% Cl	unnamed Fe–Mn-chloride
SX_9	rhombic	colourless	high	high	daughter phase	Ca, Mn, Fe, O	carbonate mineral
SX_{10}	tabular; rhombic	colourless	high	high	accidental trapping	Ca, O	calcite
SX_{11}	needle	opaque or brown	high	none	accidental trapping	Ti, O	rutile
SX_{12}	??	green–brown	high	none	accidental trapping	??	??
SX_{13}	hexagonal prism	colourless or yellow	high	??	accidental trapping	??	??
SX_{14}	??	colourless	moderate	high	accidental trapping	??	??
SX_{15}	round	colourless or brown	low	none	accidental trapping	??	??

*Solid phases present in the majority of inclusions observed and showing consistent volumetric fill ratios (solid:inclusion volume) are considered true daughter phases. Daughter phases SX_5, SX_7 and SX_9 did not dissolve upon heating (see text for discussion of this behavior)

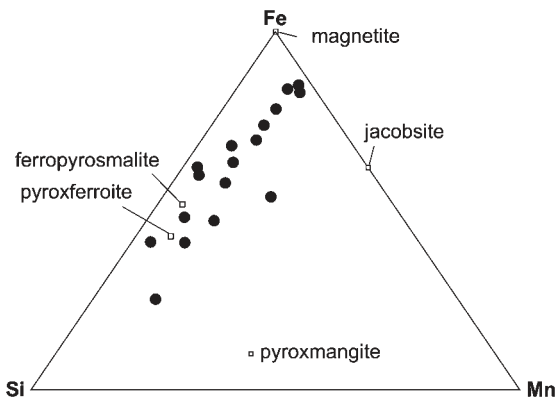

Fig. 4. Semi-quantitative SEM-EDS analyses (mol %) of daughter phase SX_7 from type I inclusions plotted on an Fe–Si–Mn ternary compositional diagram. □, locations of end-member mineral compositions. Analyses of daughter phase SX_7 (•) plot in a wide compositional field between end-member ferropyrosmalite, pyroxferroite and magnetite–jacobsite solid solution.

inclusions in single assemblages is unambiguous evidence for the heterogeneous entrapment of two immiscible fluid phases (i.e. aqueous brine and carbonic fluid; Roedder, 1984). In graphic quartz near the contact with the margin zone of the pegmatite (Fig. 8b), type I–II–III assemblages occur in concentric, planar features, together with solid inclusions of calcite. These features mimic the outer faces of the quartz crystals, suggesting that they are growth zones and indicating a primary origin for the inclusions (Goldstein, 2003). Inclusions along single growth zones vary from CO_2-dominated to brine-dominated. At the contact between the graphic quartz and massive quartz, and in the massive quartz (Fig. 8c and d), type I–II–III inclusions are coaligned forming a weak inclusion 'lineation'. These lineations are not planar features, although some rare early secondary trails occur at an angle to the main inclusion lineation (Fig. 8c and d). Rather, the longest inclusion axis appears to be parallel to the direction of quartz growth and many inclusions (Figs 3c and 8d) have one end with a slight tapering ('thorn' shape); both of these features are strongly suggestive of a primary origin (Roedder, 1984; Goldstein, 2003). In the massive quartz core the inclusion lineation is distinct (Fig. 8d).

Microthermometry

Microthermometric data were obtained for most fluid inclusion types in single inclusion assemblages. These are summarized in Table 4. For secondary inclusions data are

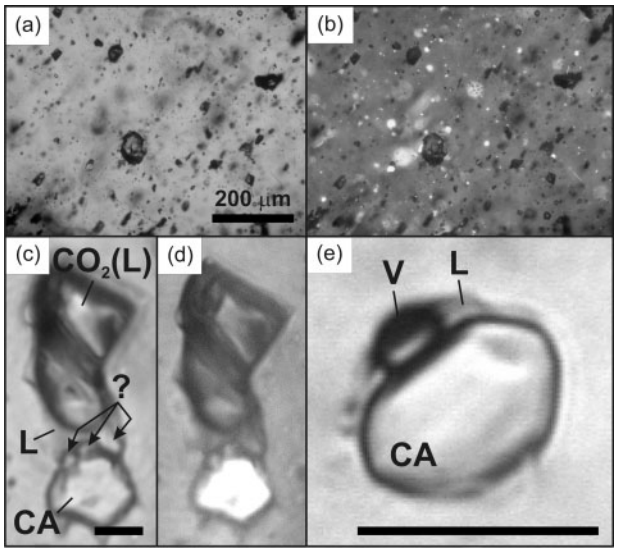

Fig. 5. Photomicrographs showing accidental calcite trapped in pegmatite quartz. Scale bars represent 10 μm unless otherwise indicated. (a) Plane-polarized light image showing inclusion-rich massive quartz. (b) Cross-polarized image of the same field of view as in (a), showing abundant, birefringent crystals of calcite included in both the quartz and fluid inclusions. (c) Plane light image (20°C) of a type III inclusion (brine, CO_2 > 50 vol. %) inclusion containing brine (L), CO_2 liquid [CO_2(L)], various other solids (question mark) and a large, accidental calcite crystal (CA). (d) Cross-polarized image of the same inclusion as in (c), showing the birefringent calcite grain. (e) Plane light image (20°C) of a small type I inclusion containing a large calcite crystal (CA) as evidence for accidental entrapment.

reported for single trails. For primary inclusions data are reported for single growth zones in graphic quartz, or for small, texturally coeval groups of inclusions in the massive quartz.

Type I, polyphase brine inclusions

Figure 9 summarizes the microthermometric data for type I inclusions. Heating of olivine-hosted type I inclusions resulted in the dissolution of all solid phases other than SX_7 ('pyrosmalite'). During heating, olivine oxidation prevented accurate observation of vapour bubble disappearance and the dissolution of solid phases other than halite. Halite dissolution temperatures ($T_{m,NaCl}$) were obtained for 53 inclusions yielding an average temperature of 480 ± 52°C (n = 53; ±1σ; range = 412–601°C). Using the relationship between $T_{m,NaCl}$ and fluid salinity (wt % $NaCl_{equiv}$) for the NaCl–H_2O system (Sterner *et al.*, 1988), the average salinity of type I inclusions in olivine is calculated to be 56 ± 6 wt % $NaCl_{equiv}$ (n = 53; ±1σ; range = 48–70 wt % $NaCl_{equiv}$). Vapour bubble disappearance ($T_{H2O,L+V>L}$) is reported for only 15 of the 53 measured inclusions in olivine. The average vapour bubble disappearance temperature ($T_{H2O,L+V>L}$) in olivine-hosted type I inclusions was 411 ±27°C (n = 15; ±1σ;

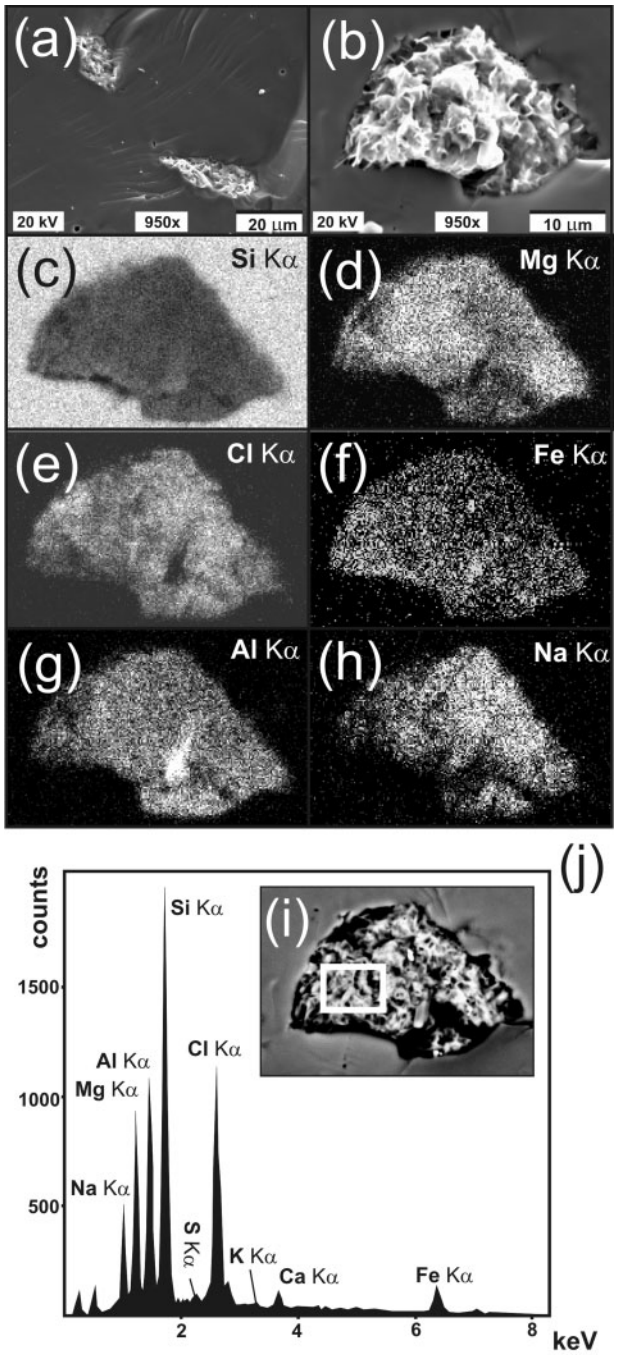

Fig. 6. Type VI (chlorosilicate melt) inclusions in graphic quartz from the pegmatite. (a) SEM (secondary electron) image of two opened type VI inclusions; small holes are type II inclusions. (b) SEM (secondary electron) image of opened type VI inclusion showing an aggregate of tiny platy crystals. (c–h) X-ray maps (EDS) showing the intensities of Si, Mg, Cl, Fe, Al, and Na *K*α of the inclusion shown in (b). The homogeneous composition of the inclusion apart from Al, which shows a zone of enrichment where a contaminating particle of alumina powder is lodged in the inclusion, should be noted. (i) SEM (back-scattered electron image) of the opened type VI inclusion. (j) SEM-EDS spectrum of the area outlined in (i) showing the Cl-rich composition of the polycrystalline contents of the inclusion.

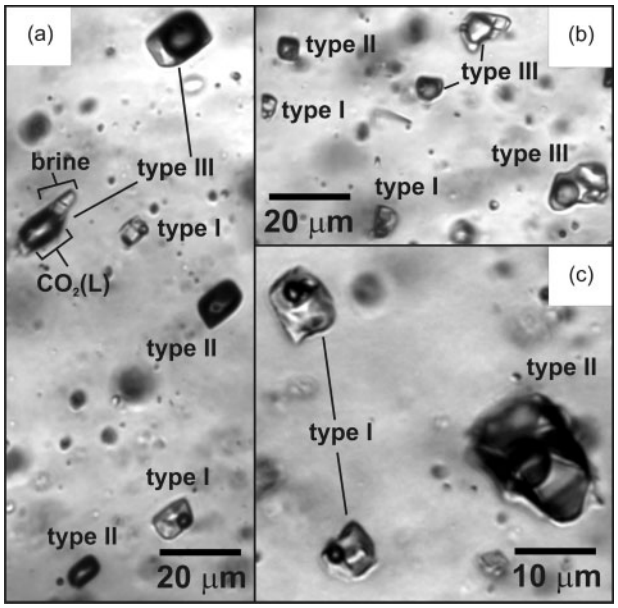

Fig. 7. (a–c) Photomicrographs [all at 20°C, except for (c) at −10°C] of coexisting type I (brine), type II (CO_2), and type III (heterogeneously trapped brine + CO_2) in pegmatite quartz as evidence for fluid immiscibility.

range = 370–459°C). Of those 15 inclusions, two homogenized by vapour bubble disappearance and the remainder homogenized by halite dissolution.

Measurements of $T_{H2O,L+V>L}$ in the pegmatite were obtained from only 16 inclusions in the massive quartz and 19 inclusions in graphic quartz because of the metastable disappearance and reappearance of the vapour bubble. The average $T_{H2O,L+V>L}$ for type I inclusions in the massive quartz was 230 ± 43°C ($n = 16$; ±1σ; range = 166–327°C). In the graphic quartz, the average $T_{H2O,L+V>L}$ was comparable at 274 ± 55°C ($n = 19$; ±1σ; range = 178–397°C). The dissolution of solid phases other than halite was generally difficult to observe because of their size, but some data were obtained: solid SX_1 dissolved between 400 and 500°C after holding T for 15–20 min; SX_2 between 275°C and 305°C; SX_3 dissolved between 150°C and 176°C; and SX_4 at ~95°C. Some solid phases did not dissolve on heating even after holding T at 700°C for 4–5 h (solids SX_5, SX_7, and SX_9); this may be due to minor post-entrapment water loss from the inclusions (see discussion below). The last observed phase change in type I inclusions was halite dissolution ($T_{m,NaCl}$). The average $T_{m,NaCl}$ in the massive quartz was 335 ± 87°C ($n = 73$; ±1σ; range = 140–524°C), corresponding to an average salinity of 42 ± 8 wt % $NaCl_{equiv}$ ($n = 73$; ±1σ; range = 28–63 wt % $NaCl_{equiv}$; salinity equation from Sterner *et al.*, 1988). In the graphic quartz, values for $T_{m,NaCl}$ overlapped considerably with values from the massive quartz, but the range in measured values was much higher. In the graphic quartz, average $T_{m,NaCl}$ was 482 ± 53°C ($n = 122$; ±1σ; range = 399–642°C) corresponding to an average salinity of 58 ± 7 wt % $NaCl_{equiv}$ ($n = 122$; ±1σ; range = 47–79 wt % $NaCl_{equiv}$). Values of $T_{m,NaCl}$ vary between growth zones and inclusion groups. Salinities and $T_{H2O,L+V>L}$ values in the pegmatite span a large range, implying that the inclusions record a prolonged evolution (cooling, dilution) of a hydrothermal system.

Despite having a distinctly higher and narrower range of $T_{H2O,L+V>L}$ values, type I inclusions in olivine show a comparable salinity range and daughter mineral assemblage to those in the pegmatite quartz, suggesting that these inclusions contain the same brine.

Type II and III, carbonic fluid inclusions and polyphase brine–carbonic fluid inclusions

In the graphic quartz, the average CO_2 final melting temperature ($T_{m,CO2}$) is −57·0 ± 0·7°C ($n = 79$; ±1σ; range = −59·1 to −55·9°C). CO_2 inclusions in the massive quartz yielded higher average $T_{m,CO2}$ values of −56·0 ± 0·4°C ($n = 72$; ±1σ; range = −56·6 to −54·8°C) (Fig. 10a). Liquid, solid, and vapour CO_2 were all present during melting.

In the graphic quartz, $T_{m,CO2}$ values below −56·6°C (pure CO_2) indicate that additional species (e.g. CH_4, SO_2, H_2S, N_2) are present. This was confirmed by a gas chromatography (GC) analysis of volatiles released from crushed quartz at the University of Toronto (see method in Bray & Spooner, 1992), which showed that the inclusions contain a significant amount of CH_4 (1·1 mol %) and some other aliphatic hydrocarbons (0·039% $C_2H_6 + C_2H_2$, 0·004% C_4H_{10}). From the GC analysis, we conclude that CH_4 is the main species responsible for the depressed values of $T_{m,CO2}$ in the graphic quartz.

$T_{m,CO2}$ values above −56·6°C are unusual, but have been reported before in ultramafic xenoliths (Murck *et al.*, 1978; Frezzotti *et al.*, 1992), migmatites (van der Kerkhof & Olsen, 1990), and some gold deposits (e.g. Porgera, PNG; J. P. Richards, personal communication). Because we have ruled out microthermometric stage calibration errors, and the occurrence of any significant thermal gradients in the stage and samples, the observed CO_2 melting behavior in the massive quartz-hosted inclusions can only be due to the presence of an unidentified species in solid solution with the frozen CO_2 phase that has a high melting T compared with CO_2. The halocarbons tetrachloromethane (CCl_4; $T_{melting} = -23$°C) and tetrachloroethane (C_2Cl_4; $T_{melting} = -22{\cdot}4$°C) are two candidates. Assuming ideal mixing, we estimate that 3–5 wt % of halocarbons dissolved in the frozen CO_2 would be required to raise $T_{m,CO2}$ by the maximum observed 1·8°C. Although these compounds cannot be detected by GC, Mathez *et al.* (1989) computed theoretical C–O–H–Cl magmatic vapour compositions in the Stillwater Complex and found that CCl_4 may have been a minor species.

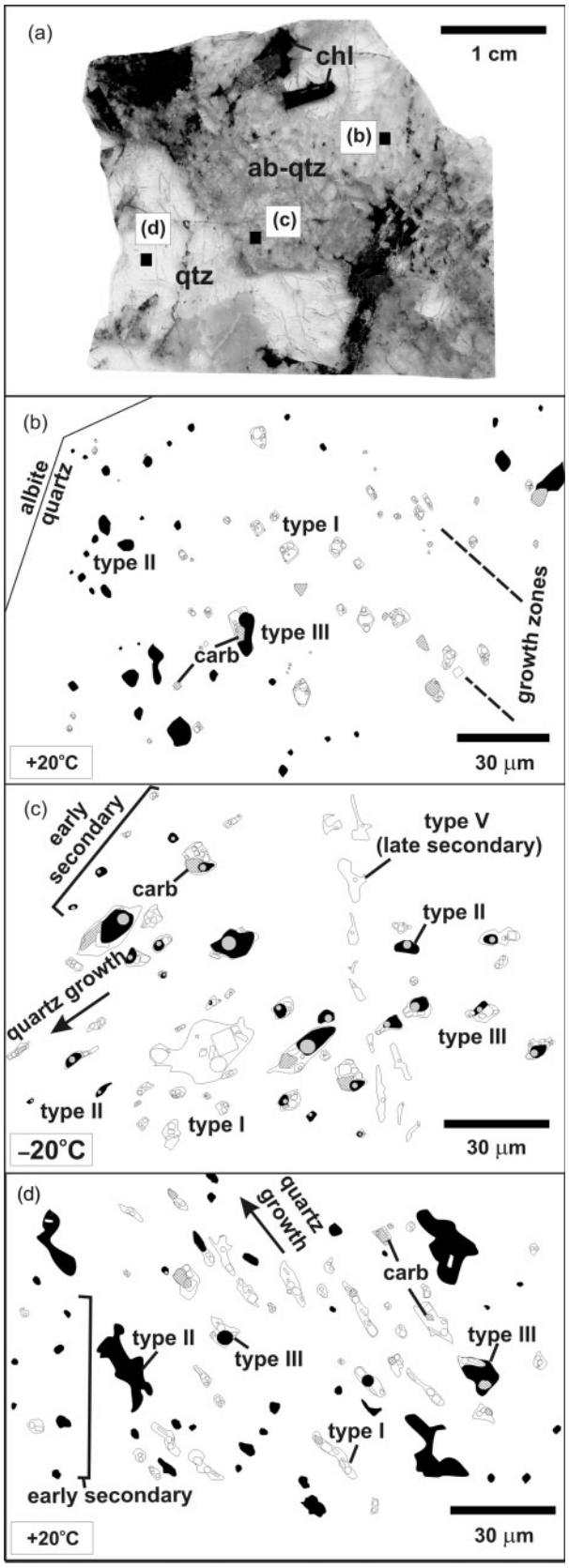

The carbonic fluid phase in all inclusions homogenizes either to a liquid (L + V → L) or to a supercritical fluid (L + V → SCF) by critical or near-critical behavior, recognized by the gradual fading or 'bubbling' of the boundary between CO_2 vapour and liquid during heating. In the massive quartz, the average CO_2 homogenization temperature (T_{CO2}) was $5 \pm 9°C$ ($n = 72$; $\pm 1\sigma$; range = −13 to 26°C); in the graphic quartz, T_{CO2} values were considerably lower, averaging $-10 \pm 8°C$ ($n = 79$; $\pm 1\sigma$; range = −28 to 2°C) (Fig. 10b). Figure 10c is a plot of T_{CO2} vs $T_{m,CO2}$ showing the range in data observed. Inclusions in single growth zones in the graphic quartz and small groups of inclusions in different areas of the massive quartz are identified in Fig. 10c. T_{CO2} and $T_{m,CO2}$ values vary from growth zone to growth zone in the graphic quartz, and from area to area in the massive quartz. The lowest $T_{m,CO2}$ values were measured in the earliest formed growth zones in the cores of the graphic quartz crystals, implying that the CH_4 content in the fluid decreased as quartz crystallization proceeded. Inclusions containing pure CO_2, indicated between the grey dotted lines in Fig. 10c, show variations in T_{CO2} values that can only reflect variability in fluid density and, consequently, the pressure of entrapment. For type II inclusions in the graphic quartz, the graphically estimated average CH_4 content of the inclusions is 2·6 mol % (Fig. 10d; Heyen *et al.*, 1982).

Fig. 8. Fluid inclusion maps from pegmatite quartz showing coeval type I–II–III inclusions and accidentally trapped calcite. Inclusion types: Black, single-phase CO_2 fluid; grey, CO_2 vapour in two-phase CO_2 inclusions; white, brine inclusions; hatched, calcite. (a) Thin section through the pegmatite core showing albite–quartz intergrowth (ab–qtz) and massive quartz. The occurrence of corroded chlorite (chl) pseudomorphs after hornblende and clinopyroxene suspended in the graphic-textured intergrowth should be noted. (b–d) correspond to locations of fluid inclusion maps as follows: (b) A fluid inclusion map drawn from a 30 μm thickness of a thin section at 20°C. Map area is in quartz from the graphic albite–quartz intergrowth. Concentric inclusion-rich zones are interpreted to be growth zones. The generally isometric and negative crystal habit of the inclusions should be noted. (c) A fluid inclusion map drawn from a 30 μm thickness of a thin section at −20°C. Map area is from the contact area between graphic and massive quartz. The more irregular or slightly elongated shape of the inclusions and weak alignment of inclusions forming a 'lineation' in the inferred direction of quartz growth should be noted; also noteworthy are a trail of early secondary brine + CO_2 inclusions occurring at a slight angle to the main inclusion 'lineation' and a cross-cutting trail of late secondary type V inclusions. (d) A fluid inclusion map drawn from a 30 μm thickness of a thin section at 20°C. Map area is from massive quartz at the core of the pegmatite. Elongate and tapered morphology of the inclusions, and strong alignment or 'lineation' in the inferred direction of quartz growth, should be noted; also, a trail of early secondary brine + CO_2 inclusions occurring at an angle to the main inclusion 'lineation'. All of the inclusion assemblages are interpreted to have a primary origin other than the early secondary I–II–III trails and late type V trails. The primary assemblages formed within crystallizing quartz (from melt in the granophyric intergrowth) or precipitating quartz (from fluid in the massive quartz core).

Table 4: Summary of fluid and melt inclusion microthermometric[1] data

Inclusion type	Host	Origin[2]	Phases present (20°C)[3]	T_e (°C)	$T_{m,CO2}$ (°C)	$T_{m,ice}$ (°C)	T_{CO2} (°C)	$T_{H2O,L+V>L}$ (°C)	$T_{m,NaCl}$ (°C)	Salinity (wt % $salt_{equiv}$)
Type I	graphic quartz	P	$L_{aq} + V_{aq}$ (<10 vol. %) + H + SX_n	–	–	–	–	274 ($n = 19$)	**482 ($n = 122$)**	58 (Na, $n = 122$)
				–	–	–	–	(55/178/397)	(53/399/642)	(7/47/79)
Type I	massive quartz	P, ES	$L_{aq} + V_{aq}$ (<10 vol. %) + H + SX_n	–	–	–	–	230 ($n = 16$)	**335 ($n = 73$)**	42 (Na, $n = 73$)
				–	–	–	–	(43/166/327)	(87/140/524)	(8/28/63)
Type I	olivine	S	$L_{aq} + V_{aq}$ (<10 vol. %) + H + SX_n	–	–	–	–	411 ($n = 15$)	480 ($n = 53$)	56 (Na, $n = 53$)
				–	–	–	–	(27/370/459)	(52/412/601)	(6/48/70)
Type II	graphic quartz	P	L_{CO2}	–	−57·0 ($n = 79$)	–	−10 ($n = 79$)	–	–	–
Type III		P	$L_{aq} + L_{CO2}$ + H + SX_n	–	(0·7/−59·1/−55·9)	–	(8/−28/2)	–	–	–
Type II	massive quartz	P, ES	(L_{CO2}, V_{CO2}) or L_{CO2} or SCF_{CO2}	–	−56·0 ($n = 72$)	–	5 ($n = 72$)	–	–	–
Type III		P, ES	L_{aq} + (L_{CO2}, V_{CO2}), L_{CO2}	–	(0·4/−56·6/−54·8)	–	(9/−13/26)	–	–	–
			or SCF_{CO2} + H + SX_n	–	–	–	–	–	–	–
Type IV	olivine	S	$L_{aq} + V_{aq}$ (<10 vol. %)	–	–	–	–	–	**760 ($n = 39$)**	95 (Na, $n = 39$)
			+ H (>90 vol. %) + SX_n	–	–	–	–	–	(40/660/800)	(4/82/100)
Type V	both types of quartz	LS	L_{aq} or $L_{aq} + V_{aq}$	−52 ($n = 6$)	–	−22 ($n = 49$)	–	**103 ($n = 43$)**	–	20 (Ca, $n = 49$)
				(3/−56/−46)	–	(14/−46/−4)	–	(19/62/145)	–	(7/6/29)
Type VI	graphic quartz	??	Cl-rich silicate melt ?	–	–	–	–	–	–	–
				–	–	–	–	–	–	–

[1]Value is the average based on *n* measurements; values in parentheses are the 1σ variability on each average value, and the minimum and the maximum value for each population. Values in bold indicate the mode of total homogenization, except for secondary (type I) inclusions in olivine, which homogenized by vapour bubble disappearance or halite dissolution.
[2]Inclusion origin: P, primary; ES, early secondary (differentiates early secondary type I-II-III inclusions and late secondary type V inclusions); S, secondary; LS, late secondary.
[3]Phases present at 20°C: L_{aq}, aqueous brine; V_{aq}, aqueous vapour; H, halite; SX_n, additional solids; L_{CO2}, CO_2 liquid; SCF_{CO2}, supercritical CO_2; V_{CO2}, CO_2 vapour. T_e, eutectic (first) melting temperature; $T_{m,CO2}$, final melting temperature of frozen CO_2; $T_{m,ice}$, final temperature melting of ice; T_{CO2}, homogenization of CO_2 to either liquid or supercritical fluid; $T_{H2O,L+V>L}$, aqueous vapour bubble disappearance temperature; $T_{m,NaCl}$, halite dissolution temperature; Salinity is salinity of the inclusions in wt % $NaCl_{equiv}$ or $CaCl_{2equiv}$ (system indicated in parentheses); maximum salinities of type IV inclusions may be slightly overestimated.

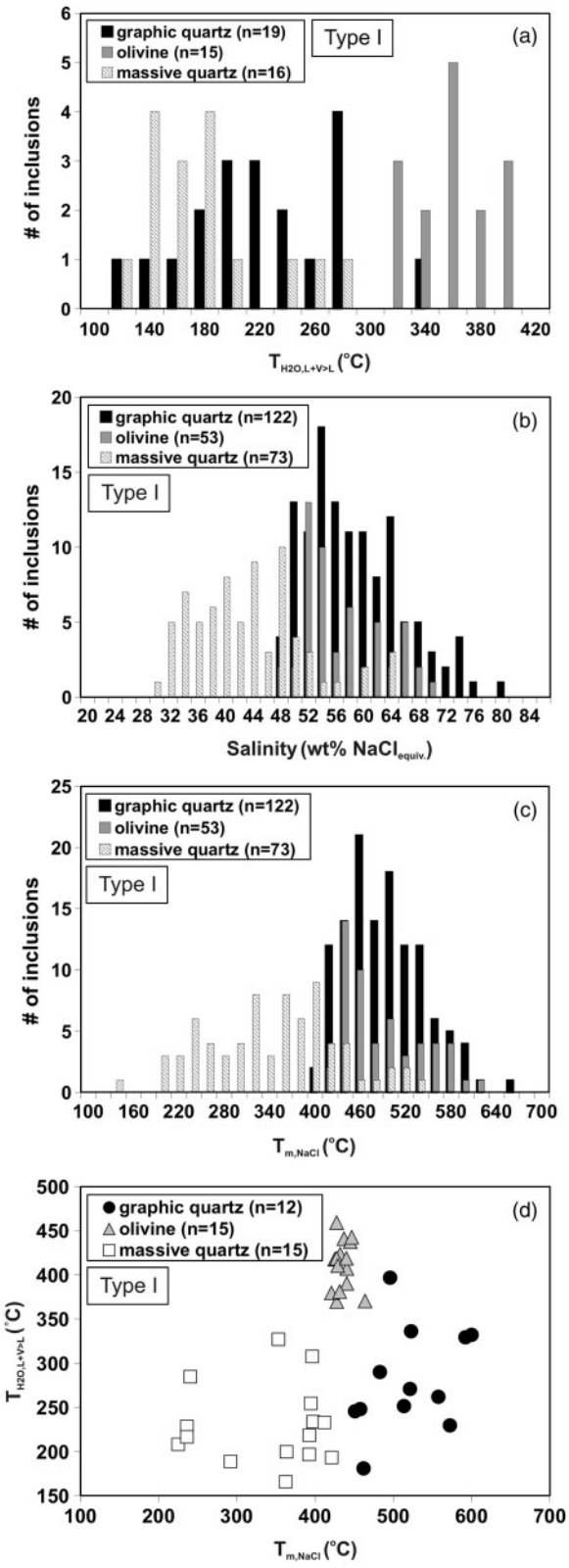

Fig. 9. Microthermometric characteristics of high-temperature phase changes for brine inclusions (type I). (a) Histogram of vapour bubble disappearance temperatures ($T_{H2O,L+V>L}$) for type I inclusions in olivine and quartz. (b) Histogram of calculated salinities (wt % $NaCl_{equiv}$) for type I inclusions in olivine and quartz. (c) Histogram of halite dissolution temperatures ($T_{m,NaCl}$) for type I inclusions in olivine and quartz; the overlap in $T_{m,NaCl}$ (and salinity; see below) between type I inclusions in olivine and those in the graphic quartz should be noted. (d) Plot of $T_{H2O,L+V>L}$ vs $T_{m,NaCl}$ for type I inclusions in olivine and quartz. Excluding a few measurements that gave anomalously high $T_{H2O,L+V>L}$ values (possibly caused by stretching), inclusions from the pegmatite show a weak positive correlation between $T_{H2O,L+V>L}$ and $T_{m,NaCl}$. Olivine-hosted type I inclusions show much higher values of $T_{H2O,L+V>L}$ than quartz-hosted type I inclusions.

Type IV, halide melt inclusions

On heating, the disappearance of the vapour bubble into the aqueous fluid rimming the solid halite and dissolution of additional phases occurred between ~300°C and ~500°C. None of these phase changes could be measured accurately because rapid heating rates were required to reach the melting temperature range of the halide melt before the olivine oxidized. The onset of halite dissolution or 'melting' was recognized by an increase in relief along the wall of the inclusions. The average final salt melting temperature ($T_{m,NaCl}$) was 760 ± 40°C ($n = 39$; $\pm 1\sigma$; range = 660–800°C). Using $T_{m,NaCl} = 660$°C, the minimum salinity of the type IV inclusions is estimated at ~83 wt % $NaCl_{equiv}$ (Sterner *et al.*, 1988). Melting temperatures are consistent with the presence of mainly NaCl. This was confirmed by SEM-EDS analysis. The presence of trace to minor amounts of water and other cations lowers the melting temperature of the halide melt below that for pure NaCl.

Type V, two-phase aqueous inclusions

On cooling, type V inclusions freeze between −25°C and −95°C, accompanied by the collapse of the vapour bubble when present. In inclusions where a vapour bubble was initially absent at room T, a single freezing cycle would nucleate a vapour bubble. Reheating from −100°C resulted in the inclusion contents becoming granular in appearance around −70°C, interpreted to be the formation of ice. The ice is brown in colour, indicating the presence of divalent cations such as Ca^{2+} and Mg^{2+} (Shepherd *et al.*, 1985). With continued heating, the first appearance of liquid (T_e) was observed confidently in only six inclusions (−56, −55, −53, −52, −54 and −46°C). Ice melting temperatures ($T_{m,ice}$) are highly variable from trail to trail, ranging from −46°C to −4°C (Fig. 11a). Within single trails, values for $T_{m,ice}$ are similar. Because many $T_{m,ice}$ values are below the NaCl–H_2O eutectic (−21·2°C), inclusion salinities were calculated in the $CaCl_2$–H_2O system. Inclusion salinities range from 6 to 29 wt % $CaCl_{2equiv}$. With continued heating, the inclusions homogenized to a liquid by vapour bubble disappearance. Values of $T_{H2O,L+V>L}$ were between 62°C and 145°C (Fig. 11b) and

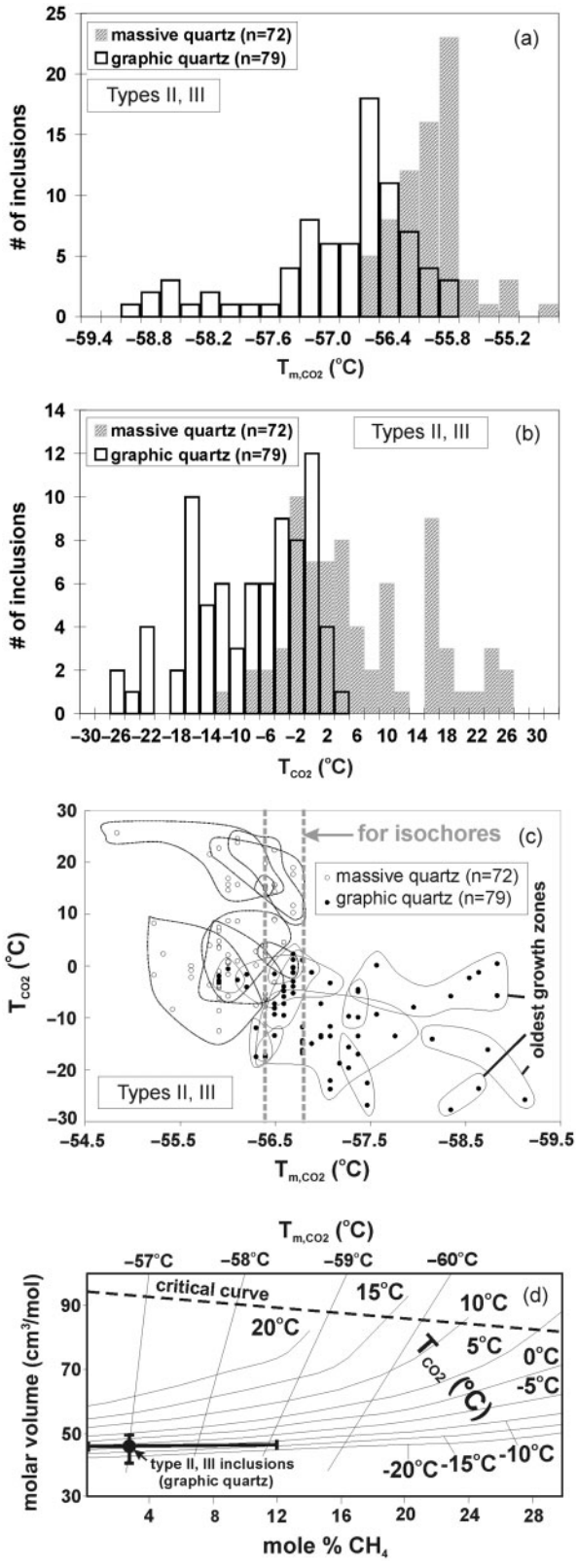

Fig. 10. Microthermometric characteristics of low-temperature phase changes, and compositional estimations for CO_2-rich inclusions (types II and III). (a) Histogram showing the range of CO_2 melting temperatures. Inclusions in the massive quartz show unusual melting behavior at or above that for pure CO_2 (−56·6°C). Inclusions in graphic quartz show a lower melting temperature range than inclusions in massive quartz, attributed to the presence of $CO_2 \pm CH_4$ (see text). (b) Histogram showing the range of CO_2 homogenization temperatures. Inclusions in the massive quartz homogenize over a larger range in temperatures than in the graphic quartz, implying a lower fluid density and lower pressures of entrapment. (c) Summary plot of T_{CO2} vs $T_{m,CO2}$ measurements for CO_2-rich inclusions (types II and III) in the massive and graphic quartz of the pegmatite. Outlines highlight inclusion groups in massive quartz or growth zones in graphic quartz, and show variability in measurements suggesting the presence of fluids varying in density and composition. The oldest growth zones are those that show the lowest $T_{m,CO2}$ values and, therefore, the highest CH_4 contents. Estimation of fluid inclusion entrapment conditions (see text) used isochores calculated from inclusions containing approximately pure CO_2 (grey dotted field; $-56{\cdot}6 \pm 0{\cdot}2$°C measurement uncertainty). (d) Estimation of molar volumes and CH_4 contents in type II and III inclusions from graphic quartz in the pegmatite core from $T_{m,CO2}$ values. Isotherms, critical curve, and axes from Heyen *et al.* (1982). •, average inclusion composition from all measurements. Filled bars show total range of measurements. From this diagram, CH_4 contents range from zero (within measurement uncertainty) to 12 mol %. The average CH_4 content is ∼2·6 mol % for all inclusions.

are similar within single trails. Salinities show an inverse correlation with homogenization temperature (Fig. 11c and d).

Whole-rock analysis

The major and trace element compositions of the margin and center of the pegmatite are listed in Table 5. Concentrations of selected incompatible trace elements are plotted in Fig. 12, normalized to primitive mantle abundances (McDonough & Sun, 1995). Plotted with the data from the pegmatite are analyses of the GNI unit hosting the pegmatite (Czamanske *et al.*, 1991; Braun *et al.*, 1994) and the estimated composition of the initial Stillwater magma from high-Mg gabbronorite dykes in the Nye Basin area (Helz, 1985). The gabbroic margin and granodioritic center of the pegmatite show similar trace element compositions, despite their contrasting mineralogical and major element compositions. The margin and center show subparallel, weakly negative-sloping rare earth element (REE) abundance patterns with the light REE (LREE) slightly more enriched relative to the heavy REE (HREE) in the center compared with the margin. Other trace elements are present in comparable concentrations in the center and margin, with the exception of: (1) Th, Nb, Ta and U, which are highly enriched in the center; (2) Co, Ni and Sc, which are moderately depleted in the center; (3) Cr, which is highly depleted in the center. Comparing the pegmatite composition with other rock types (Fig. 12), two features worth noting are: (1) the trace elements are all enriched in the pegmatite by ∼1–2 orders of magnitude relative to the host gabbronorite; (2) there is a marked similarity in composition between the pegmatite and the initial Stillwater magma.

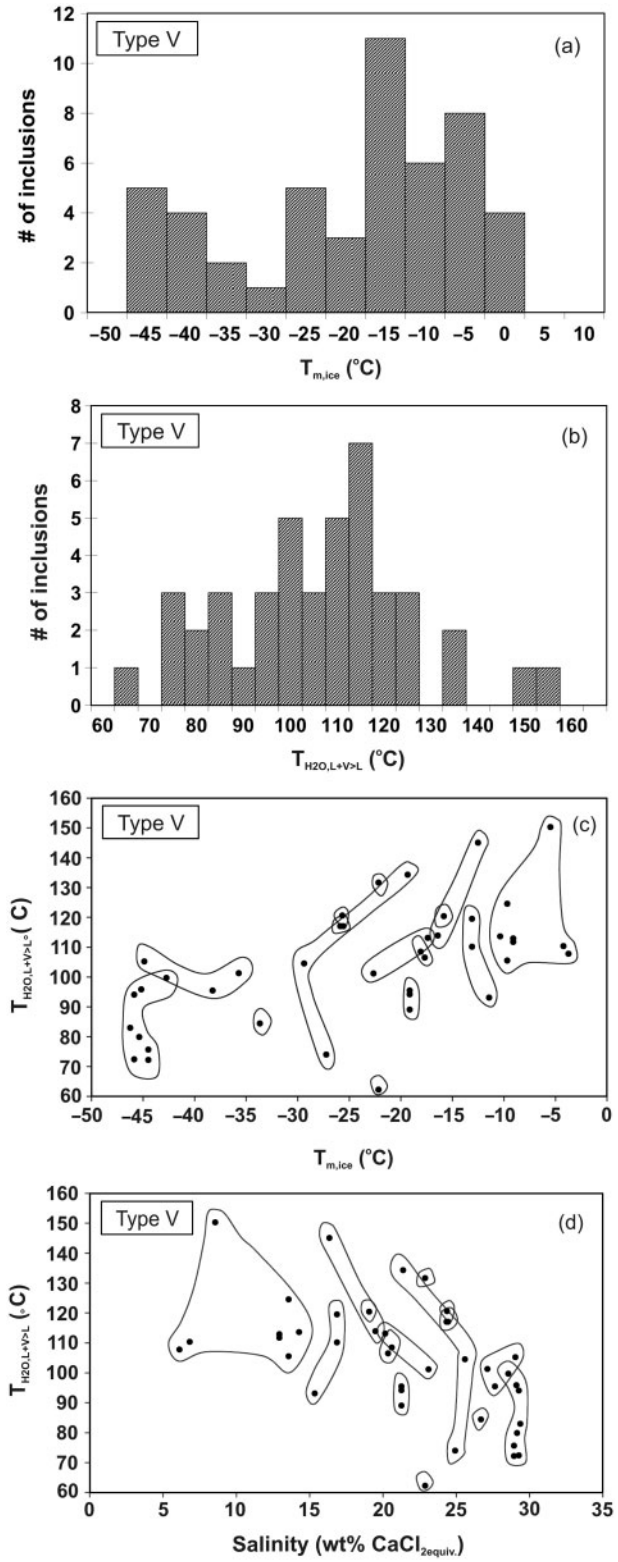

Fig. 11. Microthermometric characteristics of all phase changes for late secondary inclusions (type V). (a) Histogram showing the range of ice melting temperatures ($T_{m,ice}$). The large range in, and often exceptionally low, ice melting temperatures, indicates a continuum of dilute aqueous fluids and high-salinity brines containing divalent cations (e.g. Ca^{2+}). (b) Histogram showing the range of homogenization temperatures (=vapour bubble disappearance; $T_{H2O,L+V>L}$). (c) Summary plot of $T_{H2O,L+V>L}$ vs $T_{m,ice}$ measurements for late secondary (type V) inclusions. (d) Summary plot of $T_{H2O,L+V>L}$ vs salinity (wt % $CaCl_{2equiv}$) for type V inclusions. Outlines highlight inclusion trails, and show variability in measurements from trail to trail that suggests entrapment of fluids varying from high T, low salinity to low T, high salinity. The anticorrelation between salinity (or depression of ice melting temperature) and T should be noted.

DISCUSSION

Comparison of results with those of other studies

The fluid and melt inclusion data indicate that very Cl-rich volatile phases were present late in the crystallization history of the Stillwater Complex, and are in agreement with predicted volatile compositions from experimental (Mathez & Webster, 2005) and mineralogical studies (e.g. Boudreau *et al.*, 1986). The fluid and melt inclusion assemblages in the Stillwater Complex share several key characteristics with those found in other mafic–ultramafic systems (Table 1): (1) they contain extremely high-salinity volatiles with either dissolved or coexisting immiscible carbonic fluid; (2) the high-salinity volatiles are NaCl-dominant; (3) they occur within compositionally evolved pegmatitic phases, or interstitial and post-magmatic quartz; (4) they were trapped at conditions at or slightly below the expected solidus temperatures for interstitial residual silicate melt. Volatiles in the Bushveld Complex (Ballhaus & Stumpfl, 1986; Schiffries, 1990) are most similar to those of the Stillwater Complex; in the Bushveld Complex, inclusion assemblages indicate a similar, prolonged cooling history during which the composition of the volatiles evolved from water-poor (>80 wt % $NaCl_{equiv}$ or solid antarcticite) hydrosaline melts to water-rich brines trapped with immiscible carbonic fluid.

Hydrosaline melts have been observed in a few other mafic igneous systems. Frost & Touret (1989) reported a primary assemblage of coexisting CO_2 and Na–K–Cl melt inclusions from the Sybille Monzosyenite in the Laramie Anorthosite Complex, Wyoming, USA. Renno *et al.* (2004) reported coexisting Cu-sulfide, Cu-chloride, and silicate glass within a magnesiohastingsite cumulate from the TUBAF seamount, Papua New Guinea. Alkali halide melts have been reported in a variety of felsic and ultramafic xenoliths, as well as in kimberlites (De Vivo *et al.*, 1995; Kamenetsky *et al.*, 2004*b*; Klemme, 2004). Hanley *et al.* (2005) reported inclusions of Cu-rich, NaCl melt associated with sulfide deposits at the Sudbury Igneous Complex, Ontario, Canada. Hydrous salt melts have also been postulated as having an important role in granulite-facies metamorphism (Newton *et al.*, 1998). Many of the workers listed above have argued a

Table 5: Whole-rock analyses of the granophyric center and gabbroic margin of pegmatite SW02

	center	margin	(center/margin)*		center	margin	(center/margin)
SiO_2 (wt %)	74·28	50·94	1·5	Li (ppm)	4·4	7·9	0·6
TiO_2	1·47	0·64	2·3	Cs	0·54	0·61	0·9
Al_2O_3	12·47	21·95	0·6	Rb	24·6	31·6	0·8
Fe_2O_3	1·59	4·95	0·3	Ba	385·5	155·3	2·5
MgO	1·08	5·29	0·2	Sr	60·9	139·5	0·4
MnO	0·04	0·09	0·4	Th	14·0	0·8	16·7
CaO	2·93	11·45	0·3	U	2·2	0·35	6·3
Na_2O	3·00	1·98	1·5	Nb	13·7	3·3	4·2
K_2O	1·49	0·73	2·0	Ta	0·80	0·20	4·0
P_2O_5	0·28	0·10	2·8	Zr	60·5	43·7	1·4
LOI	1·93	2·59	0·7	Hf	2·2	1·3	1·7
Total	100·6	100·7	—	Y	17·9	13·3	1·3
La (ppm)	17·7	6·8	2·6	Mo	0·39	0·25	1·6
Ce	37·7	13·5	2·8	W	2·2	1·8	1·3
Pr	4·6	1·8	2·6	Be	0·56	0·33	1·7
Nd	18·7	8·1	2·3	Cu	45·7	31·7	1·4
Sm	4·1	2·1	1·9	Pb	7·4	15·6	0·5
Eu	0·71	0·69	1·0	Sb	0·34	0·51	0·7
Gd	4·2	2·6	1·6	Sn	1·8	1·8	1·0
Tb	0·61	0·42	1·5	Ga	9·7	16·2	0·6
Dy	3·5	2·6	1·3	Co	4·8	27·2	0·2
Ho	0·67	0·51	1·3	Ni	17·2	99·0	0·2
Er	1·8	1·4	1·3	Zn	15·8	30·3	0·5
Tm	0·25	0·19	1·3	Sc	9·1	29·6	0·3
Yb	1·5	1·1	1·4	Cr	27·8	>400	0·07†
Lu	0·23	0·16	1·4	V	121·5	157·0	0·8

*Concentration ratio between center and margin.
†Maximum (center/margin) ratio for Cr.

magmatic origin for the melt inclusions and suggested that such melts formed by exsolution from crystallizing sulfide or silicate liquids followed by inclusion entrapment in crystallizing mineral phases or interstitial glass.

Constraints on the conditions of inclusion entrapment

Estimates of the trapping conditions for fluid and melt inclusion assemblages observed in this study were made by graphical interpretation of the microthermometric data on a P–T section for the NaCl–H_2O system (Table 6; Fig. 13; Sourirajan & Kennedy, 1962; Bodnar, 1994). Plotted in Fig. 13 is the estimated maximum emplacement pressure for the Stillwater Complex based on analysis of contact-metamorphic assemblages at the base of the complex (~4 kbar; Labotka, 1985). Also shown in Fig. 13 is a

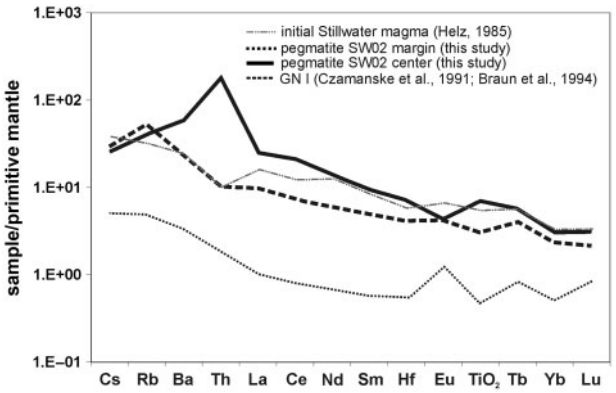

Fig. 12. Trace element abundance patterns (normalized to primitive mantle; McDonough & Sun, 1995) for the pegmatite margin and center, compared with the compositions of the host gabbronorite (GN I: Czamanske *et al.*, 1991; Braun *et al.*, 1994) and the initial Stillwater magma composition (Helz, 1985). Two features are noted: (1) the overall enrichment in all listed trace elements in the pegmatite relative to the host gabbronorite; (2) the similarity in composition between the pegmatite and the initial Stillwater magma.

Table 6: Trapping conditions estimated for fluid and melt inclusions observed in this study

Inclusion type	Host	P range (kbar)	T range (°C)	Basis for trapping P, T estimate
Type I–II–III	graphic quartz	4·3–5·6	700–715	intersection of min/max CO_2 isochores with albite–quartz–H_2O melting curve
Type I–II–III	massive quartz	1·4–4·0[1]	275–560[1]	intersection of min/max CO_2 isochores with min/max brine isochores[2]
Type I	olivine	1·5–5·5	480–640	intersection of isochores with hydrostatic and maximum lithostatic pressure estimates
Type IV	olivine	??[3]	$660_{(min)}$–$800_{(min)}$	halite melting temperatures
Type V	quartz	1–2·5	125–225	intersection of min/max isochores with P range for regional metamorphism[4]
Type VI	quartz	??	?? (low)	Cl-rich composition implies a relatively low melting T

[1]Maximum brine isochore.
[2]Assumes that brine and CO_2 were not trapped on a two-phase curve (solvus).
[3]Unconstrained.
[4]Isochores for secondary (type V) inclusions (unrelated to primary fluid assemblages in quartz).

calculated hydrostatic pressure (HP) of 1·2 kbar assuming a 12 km overburden, and the water-saturated melting curve for the albite–quartz eutectic from experimental data (Holtz *et al.*, 1992). Maximum and minimum halite dissolution temperatures ($T_{m,NaCl}$) are shown in Fig. 13 as halite liquidi (dashed sub-vertical lines).

Statement concerning post-entrapment inclusion modifications

It is necessary, before a meaningful estimation of trapping conditions is made, to evaluate whether the fluid inclusions at Stillwater suffered from any significant post-entrapment modifications in density, salinity and daughter phase assemblages resulting from inclusion stretching or shrinkage, leakage of H_2O or CO_2, or diffusion loss of H_2O and H_2. The presence of specific 'oxidized' daughter phases (carbonate, sulfate, oxide) in the Stillwater inclusions that do not dissolve after prolonged heating is evidence that some post-entrapment modification involving diffusion loss of H_2 has taken place (Mavrogenes & Bodnar, 1994). However, Mavrogenes & Bodnar (1994) pointed out that perturbations in the internal oxygen fugacity do not need to be measurable to precipitate non-dissolving daughter phases. Like H_2 loss, diffusion loss of H_2O may have also caused minor modifications to the original salinities of brine inclusions.

Nonetheless, there several lines of evidence that suggest that post-entrapment modifications have not significantly influenced the P–T–X characteristics of the inclusions. First, salinities and vapour bubble disappearance temperatures are consistent within single brine inclusion assemblages. Microthermometric characteristics vary from

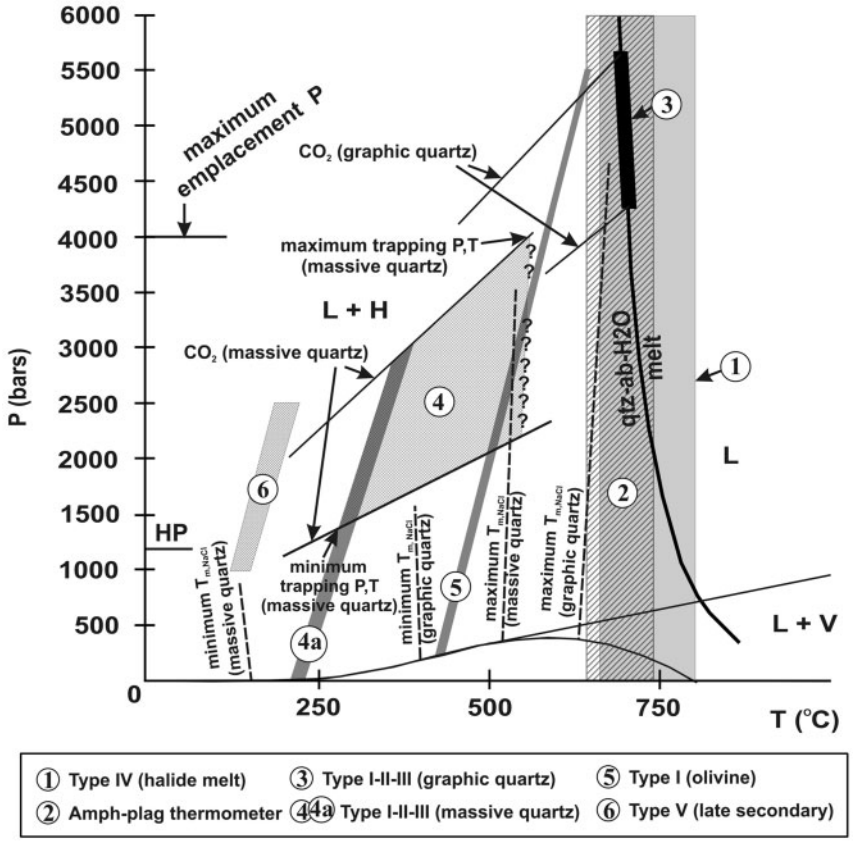

Fig. 13. Estimation of trapping conditions for fluid and melt inclusion assemblages identified in the Stillwater Complex in this study. The P–T space and various phase fields and boundaries for the NaCl–H_2O system are taken from Sourirajan & Kennedy (1962) and Bodnar (1994). The maximum pressure of intrusion emplacement is from Labotka (1985), and hydrostatic pressure (HP) is based on a 12 km thick overburden. The H_2O-saturated albite–quartz eutectic melting curve is shown in bold (Holtz *et al.*, 1992). Field '1' is the range of minimum entrapment temperatures for type IV (halide melt) inclusions in olivine. Field '2' is the range in temperatures obtained from hornblende–plagioclase thermometry including the ±40°C thermometer uncertainty. Field '3' is the range of entrapment conditions for the immiscible brine–CO_2 assemblages in the graphic albite–quartz intergrowth at the center of the pegmatite (4·3–5·6 kbar; 700–715°C). Field '4' is the range of entrapment conditions estimated for the immiscible brine–CO_2 assemblages in the massive quartz. Calculated isochores for type I brine inclusions that showed $T_{H2O,L+V>L} \approx T_{m,halite}$ are labeled as field '4a'. Field '5' is the range of isochores for type I brines in olivine. Field '6' shows the estimated range in trapping conditions for late secondary (type V) inclusions from a subsequent metamorphic overprint. The basis for the estimates of trapping conditions is discussed in detail in the text and summarized in Table 6.

growth feature to growth feature and are clearly related to trapping time and quartz type. If significant post-entrapment modifications had occurred, these should have affected large groups of inclusions in single quartz crystals, eliminating any microthermometric distinction between growth features. Second, brine inclusions were trapped in graphic quartz that grew directly from a silicate liquid and have a primary origin. Therefore, the temperatures of entrapment for these inclusions must be much higher than the low vapour bubble disappearance temperatures measured. The difference between $T_{H2O,\ L+V>L}$ and $T_{m,NaCl}$ for brine inclusions in graphic quartz is far too large to be the result of post-entrapment H_2O loss, and the high halite dissolution temperatures observed are not unreasonable. Third, there is no physical evidence outside of the inclusions to suggest that H_2O loss took place. Decrepitation haloes are absent, and there is no indication from the morphology of inclusions and the surrounding quartz that the inclusions leaked.

Trapping conditions for brine–carbonic fluid assemblages (type I, II, and III inclusions)

To estimate the trapping conditions for the brine–CO_2 assemblages in the pegmatite, the following observations are relevant: (1) CO_2 liquid or supercritical fluid was trapped coevally with brine on the basis of petrographic evidence for heterogeneous entrapment of immiscible fluid phases; (2) the carbonic fluid in a number of inclusions in the graphic-textured and massive quartz is pure CO_2 on the basis of CO_2 final melting temperatures; (3) the brine is NaCl-dominated and its P–T behavior may be approximated in the pure NaCl–H_2O system; (4) the inclusions are primary in origin.

Unfortunately, there is no theoretical knowledge or experimental data for isochores in the halite-saturated portion of the NaCl–H_2O system. Therefore, isochores for the brine inclusions in the graphic quartz are not defined, as these inclusions homogenize by halite dissolution. However, CO_2 isochores for inclusions containing pure CO_2 are well defined and these may be used to estimate the range of P–T conditions of entrapment, as brine and CO_2 inclusions in single assemblages were trapped at the same time. Densities and corresponding isochores for those inclusions containing nearly pure CO_2 (based on microthermometric behavior) were calculated using an equation of state from Saxena & Fei (1988). The intersections of the calculated minimum and maximum CO_2 isochores with the water-saturated albite–quartz melting curve are shown in Fig. 13. It should be noted that the CH_4 content of the carbonic fluid gradually increased over the crystallization history of the graphic quartz. However, because the density of pure CO_2 will be similar to that of a mixture of CO_2 and minor CH_4, the calculated isochores for inclusions containing pure CO_2 can be applied to estimating entrapment conditions for all the brine–carbonic fluid inclusions trapped in the graphic quartz with minimal error.

By this method of estimation, the brine–CO_2 assemblages in the graphic quartz were trapped between 4·3 and 5·6 kbar, and 700 and 715°C (field labeled '3' in Fig. 13). It should be noted that the highest temperature of halite dissolution in the graphic quartz assemblage was 642°C (Table 4), corresponding to a salinity of ~79 wt % $NaCl_{equiv}$. At such high salinities, halite liquidi (dashed lines; Fig. 13) have a positive slope and may intersect or pass just to the left of the field of conditions of entrapment (field '3'; Fig. 13). Therefore, the highest salinity inclusions in the graphic quartz must have been trapped very close to halite-saturated conditions. It should be noted also that lower end of the $P_{trapping}$ estimate (4·3 kbar) coincides closely with the estimated maximum lithostatic pressure for the emplacement of the intrusion. It is unclear why the upper $P_{trapping}$ estimate is considerably higher than the maximum lithostatic pressure determined from the composition of contact metamorphic assemblages at the base of the intrusion. We are confident that carbonic fluid inclusions are a robust indicator of entrapment pressure. Metamorphic assemblages, on the other hand, may have retrograded if prolonged cooling of the base of the intrusion coincided with uplift and/or removal of volcanic overburden.

For the brine–carbonic fluid inclusion assemblages in the massive quartz, entrapment conditions were constrained by the method of intersecting isochores (Roedder & Bodnar, 1980). This method can be applied only to coeval fluids that were not trapped on a two-phase curve; the brine–carbonic fluid assemblages appear to meet that criterion (see discussion in the following section). Like the type I inclusions in the graphic quartz, vapour bubble disappearance temperatures for type I inclusions in the massive quartz were usually much lower than halite dissolution temperatures. For those inclusions, the 'vapour-out' point for the isochore is well defined on the bubble curve by the vapour bubble disappearance temperature, but the slope of the isochore beyond the bubble point cannot be constrained in the halite-saturated field because of a lack of theoretical knowledge or experimental data for the NaCl–H_2O system in that region. However, a minimum P–T constraint for entrapment of the brine–carbonic fluid assemblages in the massive quartz can be estimated by finding the intersection of the lowest density CO_2 isochore with the isochores for brine inclusions in which $T_{m,NaCl} \approx T_{H2O,L+V>L}$. For those brine inclusions, isochores could be calculated using an equation of state from Zhang & Frantz (1987) and are shown in Fig. 13 (field labeled '4a'). The intersection defines a minimum entrapment condition of about 1·4 kbar and 275°C. The minimum pressure estimate is comparable with the estimated hydrostatic pressure (~1·2 kbar), suggesting that the

pegmatite core was part of an open-to-surface fracture system during the final stages of fluid entrapment.

A maximum P–T constraint of entrapment for the inclusion assemblages in the massive quartz could not be made because all of the highest salinity brine inclusions from the massive quartz homogenized by halite dissolution. However, two observations allow for an approximation of the maximum entrapment conditions. First, the entrapment conditions must lie between the minimum and maximum CO_2 isochores at a temperature above the maximum halite dissolution temperature measured in the massive quartz ($T_{m,NaCl} = 524°C$; ~63 wt % $NaCl_{equiv}$; Fig. 13). Second, because the density of the brine is very high and the isochores in the liquid-only field are therefore likely to be steep, the maximum entrapment conditions cannot be much higher in T than the intersection of the maximum CO_2 isochore and the 63 wt % halite liquidus. This intersection occurs at T and P of approximately 560°C and 4 kbar, respectively (Fig. 13). Combining these observations, the brine–carbonic fluid assemblages in the massive quartz were probaby trapped over a very large range of conditions (field labeled '4' in Fig. 13; 1·4–4·0 kbar; 275–560°C). The range in entrapment conditions is consistent with the zonation in microthermometric characteristics of brine inclusions in the massive quartz, and probably indicates an evolving hydrothermal system in which the brines became cooler and less saline with time as quartz-infilling took place.

Overall, the estimates of trapping conditions for primary inclusions in the pegmatite indicate prolonged hydrothermal activity. Inclusions record the transition from the crystallization of residual silicate melt that trapped high-T brine–carbonic fluid at lithostatic P, to lower T conditions at which brine–carbonic fluid migration occurred through an open conduit at hydrostatic P.

Trapping conditions for brine and halide melt inclusions in olivine

Isochores for several type I inclusions in olivine could be calculated using the equation of state from Zhang & Frantz (1987). The field of isochores for type I inclusions in olivine is shown in Fig. 13 (labeled '5'). In the absence of coeval CO_2 inclusions, only an approximate constraint on trapping conditions can be made where the brine isochores intersect hydrostatic pressure and lithostatic pressure. The trapping conditions are poorly constrained in the range 1·5–5·5 kbar and 480–640°C. It is more likely that the inclusions in the olivine were trapped at the higher T end of the estimated P–T range, as the olivine and its host rocks are devoid of any hydrous alteration.

Only a range of minimum entrapment T of 660–800°C can be estimated for type IV inclusions containing the halide melt phase. This range corresponds to the range in $T_{m,NaCl}$ measured in the inclusions, and overlaps with the estimated entrapment temperatures for the brine–carbonic fluid assemblages in the graphic quartz.

Trapping conditions for the silicate melt inclusions

No microthermometric data were obtained for the unusual type VI inclusions because of their rarity. Other than Fe and Mg, the composition of the crystalline material inside the inclusions resembles a variety of unusually Cl-rich, cancrinite-group minerals that are known to form through the metasomatic reaction of high-salinity brines with rock of andesitic or basaltic composition; this group includes quadridavyne, containing 12 wt % Cl [$(Na,K)_6Ca_2Al_6Si_6O_{24}Cl_4$] and microsommite, containing 7·5 wt % Cl [$(Na,Ca,K)_{7-8}(Si,Al)_{12}O_{24}(Cl,SO_4)_{2-3}$] (Merlino *et al.*, 1992; Bonaccorsi *et al.*, 1994). The high Cl content and abundance of a variety of alkalis in the inclusions imply that the melting temperature of the crystalline phase is probably low.

Independent constraints of fluid entrapment temperatures in the pegmatite

Coarse-grained hornblende and plagioclase in the margin of the pegmatite are in textural equilibrium. Thus, their compositions may be used to estimate the T of final equilibration associated with fluid-augmented recrystallization of the GNI unit and pegmatite formation by applying the hornblende–plagioclase thermometer of Holland & Blundy (1994). Over a pressure range of ~4·3–5·6 kbar, estimated as the range in pressure of entrapment for the brine–CO_2 assemblages in the graphic-textured quartz, the amphibole–plagioclase thermometer yields a T range of 676–705°C (±40°C). This range in temperature is entirely consistent with an expected solidus temperature of the graphic albite–quartz intergrowth of ~700°C at 5·5 kbar at fluid-saturated conditions (Holtz *et al.*, 1992). The upper T limit is also consistent with the presence of Mg-chlorite in the pegmatite center that decomposes above 760°C at $P = 5·5$ kbar (Jenkins & Chernosky, 1986). The range in T determined using the mineral thermometer is shown in Fig. 13.

Evidence for brine–carbonic fluid immiscibility and disequilibrium entrapment

Based on the estimates of fluid inclusion entrapment conditions in the pegmatite, the inclusion assemblages at Stillwater preserve evidence of heterogeneous entrapment of immiscible aqueous brine and CO_2 over a very wide range of P–T–X conditions. An outstanding question concerns the exact origin of these immiscible fluid phases.

An initially one-phase NaCl–CO_2–H_2O fluid will unmix into CO_2-dominant and NaCl–H_2O-dominant fluids. The two-phase field and its associated bounding solvus curve expands significantly to higher temperatures

as the total salinity of the system increases. At very high salinities (i.e. 50–70 wt % NaCl), the two-phase field may extend to at least 930°C and 7 kbar (Bowers & Helgeson, 1983; Frantz *et al.*, 1992; Joyce & Holloway, 1993; Duan *et al.*, 1995). At the conditions estimated for the entrapment of brine–CO_2 assemblages in the graphic quartz (maximum 715°C and 5·5 kbar) and the very high salinity of the brine component, near-complete immiscibility would have restricted the solubility of coexisting fluid phases in one another to less than 5 mol % (Frantz *et al.*, 1992; Joyce & Holloway, 1993).

However, this certainty of brine–CO_2 immiscibility does not mean that the fluid components were originally part of a single-phase fluid that unmixed. In fact, the microthermometric data prohibit this. Brine inclusions trapped with carbonic fluid inclusions in the pegmatite homogenize by halite dissolution at much higher temperatures than the vapour bubble disappearance. In fluid inclusion assemblages where only single-phase brines occur, this behavior is allowable at specific P–T conditions in the NaCl–H_2O system (Roedder & Bodnar, 1980). However, when fluid inclusion assemblages contain coeval, high-density brine and lower density vapour that unmixed from a single fluid, this homogenization behavior is not permissible. Where unmixing has occurred, the high-salinity inclusions must homogenize by vapour bubble disappearance if they were trapped in equilibrium with the associated low-density phase on the limbs of a solvus (Roedder & Bodnar, 1980).

At Stillwater, it is more likely that brine and carbonic fluid exsolved separately from interstitial silicate melts occurring at different depths in the cumulate pile. At a given CO_2 and H_2O content in a melt, CO_2 should exsolve first because its solubility is much lower than that of Cl (Webster *et al.*, 1999; Webster, 2004). Therefore, the carbonic fluid may have exsolved from a hotter, shallower portion of the cumulate pile where the interstitial liquid was CO_2 saturated. At a deeper level in the igneous pile, cooler, interstitial silicate liquid exsolved a more hydrosaline fluid because it had already lost CO_2 at an earlier crystallization stage. These two distinct fluids were physically trapped together in the pegmatite that had acted as a common flow path for both fluid end-members, but were never in chemical equilibrium and originated from different parts of the cooling intrusion.

It could be argued that the brine inclusions in the olivine represent a single-phase brine that unmixed to form the brine and CO_2 that are observed in the pegmatite higher in the stratigraphy; brine inclusions in the olivine and massive quartz have very similar compositional and microthermometric characteristics. However, a bulk GC analysis of the volatiles released from type I inclusions in crushed olivine from sample UM4 yielded a low CO_2 content of 0·88 mol %. At this low CO_2 content, CO_2 would not unmix from a single-phase brine until very low P and T very low P and T (Joyce & Holloway, 1993). It is more likely that brine–CO_2 inclusions are not observed in olivine because CO_2 was not mingling with the brine end-member in that area of the cumulate stratigraphy. Alternately, the wetting properties of CO_2 on olivine may have prevented co-entrapment of carbonic fluid.

The origin of the high-salinity brines and halide melts

Having ruled out any significant post-entrapment modifications, how can such hypersaline fluids phases evolve in a layered intrusion? Although the processes that control the exsolution and composition of the hydrosaline magmatic volatile phase are well constrained in felsic systems (e.g. Roedder & Coombs, 1967; Shinohara *et al.*, 1989; Lowenstern, 1994; Shinohara, 1994; De Vivo *et al.*, 1995; Williams *et al.*, 1995; Webster 1997; Webster *et al.*, 1999; Kamenetsky *et al.*, 2004*a*; Webster, 2004), they are not well characterized in mafic systems. Limited experimental data (Webster *et al.*, 1999) and field observations for basaltic systems show that Cl solubility varies inversely with H_2O content, and a hydrosaline liquid phase will stabilize only when Cl concentration in the melt is very high. In typical basaltic melts, in which Cl concentrations are <1 wt % Cl, the exsolved fluid will contain <4 wt % Cl. To achieve a high enough Cl/H_2O ratio to exsolve a high-salinity volatile phase, a basaltic melt must (1) crystallize or react with abundant hydrous or nominally anhydrous phases that exclude Cl from their structure, or (2) acquire an unusually high Cl content from its source region, through contamination, or by 'volatile-refining'. The extremely high salinity and relatively low water content of the exsolved volatile phases at Stillwater suggest that one or both of the above requirements were met.

Hydrous phases (phlogopite, apatite) are rare in the Stillwater Complex and would have had little influence on the volatile budget as they crystallized. However, pyroxene and olivine are abundant below the J-M reef and these may incorporate tens to hundreds of ppm of H_2O into their structure but exclude Cl (Bell & Rossman, 1992; Bromiley & Keppler, 2004). Mathez & Webster (2005) proposed that pyroxene may have extracted large amounts of H_2O from the silicate melt as it infiltrated thick sequences of partially crystallized cumulates. By this process, they argued that the mobile silicate liquid could achieve the high Cl/H_2O ratio necessary to exsolve a hypersaline volatile phase. The extremely Cl-rich silicate melt inclusions (type VI) observed in the pegmatites are one indication that such a dehydration process took place. Alternately, the dehydrated phase may have been a free aqueous fluid that evolved from a low-salinity fluid to a halide melt by losing water to large thicknesses of pyroxene-rich cumulates. The problem with this theory is that many

large mafic–ultramafic intrusions (e.g. Skaergaard, Great Dyke) do not contain the diagnostic mineral phases such as Cl-rich apatite and phlogopite that show that hydrosaline volatiles were formed during intrusion crystallization, despite these intrusions containing many hundreds to thousands of meters of pyroxene-bearing cumulates.

Dehydration may not be necessary if 'volatile-refining' takes place (Boudreau & Meurer, 1999; Willmore *et al.*, 2000). This process occurs when hot, interstitial silicate liquids are enriched in Cl that has exsolved from cooler, more crystallized rocks at lower levels in the igneous stratigraphy. By this process of 'volatile-refining' unusually high Cl content and Cl/H_2O ratios may be achieved in interstitial liquids. Alternately, the original Cl content of the Stillwater magma may have been unusually high. Marginal sill and dyke compositions, which are considered primary liquid compositions, contain apatite that has anomalously high Cl/F ratios compared with most other intrusions (A. Boudreau, personal communication). Boudreau *et al.* (1997) showed that halogens were enriched in the Stillwater magma during melt extraction from metasomatized, depleted mantle, and subsequently by assimilation of Cl-rich crustal materials.

Further work on these intrusions is required to confirm the mechanisms described above. It is important to note that modeling volatile compositions in layered intrusions is extremely difficult because of the nature of volatile exsolution. Because different parts of an intrusion would have cooled to different extents at any specific time in the intrusion's overall cooling history, volatile exsolution cannot be treated as a simple function of crystallization of a single batch of magma. Additionally, the record of volatile exsolution at the Stillwater Complex is contained within pegmatites that have acted as common pathways that have simultaneously trapped different fluids originating from different parts of the intrusion. Brine inclusions in the graphic quartz lend considerable support to this argument because they show significant variations in salinity when different assemblages are compared, even if those assemblages occur in single crystals (Table 4). This implies that there were large fluctuations in salinity during the entrapment of inclusion assemblages in the granophyric part of the pegmatite. Such localized variations in fluid composition may result if: (1) trapped brines exsolved from different batches of residual silicate liquid in different brine source regions; (2) brines were trapped in quartz crystallizing from different batches of residual silicate liquid; (3) inclusions trapped brines that exsolved from a single batch of silicate liquid that was undergoing successive depletion in incompatible elements with each batch of brine exsolved; (4) brine compositions were modified prior to entrapment by interaction with wall rocks; or (5) incomplete mixing occurred between different brine batches prior to entrapment.

The origin of the pegmatite

At the Stillwater Complex, colder, compositionally evolved silicate liquids infiltrated hotter, less-evolved areas of the igneous pile forming discordant bodies such as pegmatites (Braun *et al.*, 1994; Meurer *et al.*, 1997; Meurer & Boudreau, 1998; Boudreau, 1999). However, the pegmatite studied here is much more chemically and mineralogically evolved than those reported by other workers (e.g. Braun *et al.*, 1994; Meurer & Boudreau, 1998); its formation requires discussion of some additional geochemical processes previously unreported at Stillwater.

The pegmatite studied cannot represent a sample of an evolved silicate liquid derived from crystallization of the Stillwater magma. Although the pegmatite center is highly evolved in terms of its major element composition compared with its GNI host rock, its incompatible trace element composition is very similar to the starting composition of the Stillwater magma (Fig. 12; Helz, 1985). The silicate melt residue left behind after the crystallization of the primary minerals would be significantly enriched in the high field strength elements and REE because bulk cumulate–melt partition coefficients for this pyroxene- and olivine-dominated mineral assemblage should be less than unity (Arth, 1976; Fujimaki *et al.*, 1984). Instead, the albite–quartz intergrowth in the pegmatite must have grown from a residual silicate liquid allowing incompatible trace elements to be excluded from the crystallizing quartz and feldspar. The silicate melt trapped in type VI inclusions may represent this residual silicate liquid.

The fluid inclusion evidence indicates that the residual silicate liquid from which the pegmatite was formed was also fluid-saturated because aqueous brine and CO_2 were trapped in the pegmatite as it crystallized. This fluid–melt mixture was channelled through the partially crystallized layered units to form the pegmatite pipes. Brines, in particular, would have been highly mobile along intergrain boundaries in the underlying rock units, owing to their effective wetting properties (Brantley & Voight, 1989). Fluid and melt mobility would be enhanced by crystal compaction within the cooling cumulate pile (Meurer & Boudreau, 1998), which would promote the formation of continuous thin fluid and melt films along the surfaces of primary mineral grains (Tullis, 2001). As the pegmatite grew, recrystallization of the surrounding GNI unit produced the coarse-textured margin zone of the pegmatite. The similar incompatible trace element abundance patterns and trace element ratios in the margin and center of the pegmatite (Fig. 12) suggest that the margin was contaminated or metasomatized by the residual fluid–silicate melt mixture.

The pure (near end-member) albite at the center of the pegmatite could have formed by the compositional refining of an impure feldspar by the NaCl-rich brine. Albitization of plagioclase would release Ca to the fluid,

allowing precipitation of calcite in the graphic quartz and entrapment of calcite within fluid inclusions. This argument is supported by recent experimental investigations of the solubility of calcite in H_2O–NaCl solutions at low to moderate crustal pressures (2–4 kbar) and $T = 600$–$900^\circ C$; the experiments show that calcite solubility in high-salinity brines is controlled by the following equilibrium (Newton & Manning, 2002):

$$CaCl_{2,aq} + H_2O + CO_2 = CaCO_3 + 2HCl_{aq}. \quad (1)$$

A similar reaction may be written involving CH_4:

$$CaCl_{2,aq} + CH_4 + 2O_2 = CaCO_3 + 2HCl_{aq} + H_2O. \quad (2)$$

Calcite precipitation in the pegmatite would be promoted by reaction of the carbonic fluid with Ca-bearing brine. It is interesting to note that reactions (1) and (2) also produce HCl and H_2O, thereby lowering the brine salinity and generating an acid component. This is consistent with the progressive decrease in salinity observed in inclusions from the center to the core of the pegmatite. The corresponding increase in the CO_2:CH_4 ratio in the carbonic fluid with decreasing entrapment age indicates either an increase in the fO_2 imposed on the fluid during fluid entrapment, or precipitation of graphite from the carbonic fluid at its source region in the intrusion (Ohmoto & Kerrich, 1977; Volborth & Housley, 1984; Cesare, 1995).

As hydrothermal activity waned and the transition from lithostatic to hydrostatic conditions took place, brine and CO_2 continued to flow through the cooling pegmatite core. Continued quartz and calcite precipitation would occur by simple fluid cooling, decompression, and decrease in fluid salinity: at high salinities, the solubility of SiO_2 does not vary significantly as a function of pressure, but a decrease in T from 560 to 275°C (Fig. 13) and salinity from about 63 to 28 wt % $NaCl_{equiv}$ (Table 4) would decrease SiO_2 solubility by a minimum of 0·6 log units (Newton & Manning, 2000). Similarly, calcite solubility is highly sensitive to changes in P, T and salinity, and would decrease by a minimum of 0·4 log units over the range of P–T–X conditions recorded by the brine–CO_2 assemblages in the massive quartz (Newton & Manning, 2002).

Evidence for migration of late metamorphic fluids

Trails of type V inclusions record a hydrothermal event postdating the entrapment of the brine–CO_2 assemblages in the pegmatite. Eutectic and ice melting temperatures suggest that the type V fluid is rich in the divalent cations Ca^{2+} and Mg^{2+}. Unlike type I inclusions, the lack of any daughter phases in type V inclusions shows that the late fluid cannot contain high concentrations of multiple divalent cations; high concentrations of multiple cations would promote the formation of multiple daughter phases as a result of the common ion effect (Williams-Jones & Samson, 1990). In the absence of daughter phases and on the basis of the low melting and eutectic temperatures, it may be concluded that the late fluid has a relatively simple composition with only one or two cations present in low to moderate concentrations. Such a composition would be consistent with the fluid involved in or derived from calc-silicate alteration of primary Ca–Fe–Mg minerals.

The type V fluid may be related to the late Proterozoic regional metamorphism responsible for the widespread alteration observed throughout the Stillwater Complex (McCallum *et al.*, 1980, 1999; Polovina *et al.*, 2004). To estimate their trapping conditions, type V inclusion compositions were modeled in the $CaCl_2$–H_2O system. Maximum and minimum isochores for the highest and lowest density type V inclusions, respectively, were calculated from Zhang & Frantz (1987). In Fig. 14, these isochores are plotted along with the P–T fields for zeolite, prehnite–pumpellyite, albite–epidote hornfels, and lower greenschist facies (Yardley, 1989). The upper and lower P limits of the 1·7 Ga metamorphic event responsible for alteration of the layered rocks and the field of P–T conditions indicated by alteration mineral assemblages at Stillwater are shown

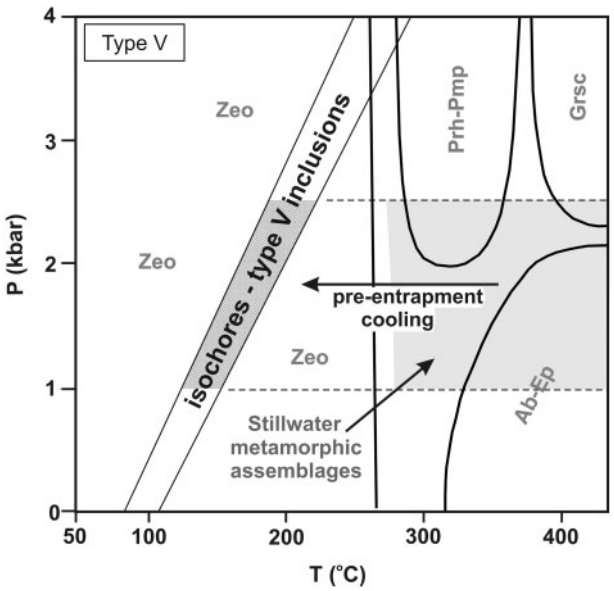

Fig. 14. Estimation of the trapping conditions for late secondary (type V) inclusions. Upper and lower P limits for the ~1·7 Ga metamorphic event responsible for alteration of the layered rocks are shown, based on estimated conditions of formation of alteration mineral assemblages reported by Polovina *et al.* (2004). Metamorphic facies P–T fields for lower greenschist (Grsc), prehnite–pumpellyite (Prh–PmP), albite–epidote hornfels (Ab–Ep), and zeolite (Zeo) are drawn from Yardley (1989). Type V inclusions contain a fluid that was trapped at conditions entirely within the zeolite field. Therefore, higher metamorphic grade fluids must have cooled significantly prior to entrapment.

(after Polovina *et al.*, 2004). Figure 14 shows that the maximum and minimum isochores for type V inclusions intersect the regional metamorphic pressure range between approximately 125 and 225°C, defining a range of entrapment conditions entirely within the zeolite field. If the type V inclusions contain fluids formed during the waning stages of metamorphism in the Stillwater Complex, then those fluids must have cooled significantly to zeolite facies conditions prior to entrapment. The fluid became concentrated in dissolved salts as temperature decreased (Fig. 11), possibly through reactions involving the formation of many of the hydroxysilicates present in the rocks of the Complex such as chlorite and prehnite. The growth of these minerals may consume large quantities of H_2O while excluding Cl during growth.

CONCLUSIONS

The data presented here are consistent with field evidence for high-temperature volatile activity in the Stillwater Complex (Boudreau *et al.*, 1986; Meurer *et al.*, 1997, 1999; Boudreau, 1999) and theoretical and experimental estimates of the expected fluid compositions (Braun *et al.*, 1994; Mathez & Webster, 2005). Fluid and melt inclusions in the Stillwater Complex provide a record of a continuum of high P–T magmatic–hydrothermal and low P–T metamorphic events. The inclusions show that residual silicate melt and two volatile phases of markedly different composition were channeled through the cumulate pile as it solidified, and the transition from lithostatic to hydrostatic pressure took place. Hydrosaline and carbonic fluids exsolved separately from different parts of the igneous pile rather than unmixing from a single-phase exsolved fluid. Fluid inclusion data constrain only the entrapment conditions for the volatiles, not the maximum temperatures at which the volatiles existed. Thus, hydrosaline and carbonic volatiles were probably present at T well above the solidus when the overlying magma chamber was still actively precipitating igneous minerals.

The data presented lend considerable support to volatile enrichment models for the formation of the J-M reef (Boudreau & Meurer, 1999). The potential for remobilization of the base metals and PGE in layered intrusions and other magmatic Ni–Cu–PGE deposits should not be dismissed on the basis of a lack of visible alteration of the mafic–ultramafic rocks hosting the deposits. In the Ultramafic Series, the absence of alteration in the orthopyroxenite hosting brine and halide melt inclusions is due to (1) chemical equilibrium between the volatiles and their surrounding host rocks, and (2) the relatively high-temperature and water-poor nature of the volatiles, preventing the stabilization of any hydroxysilicate alteration assemblages. However, if the exsolved volatiles initially had low S content, they may have been highly reactive with PGE-bearing sulfide droplets or sulfide mineral assemblages below and within the J-M reef, as S is highly soluble in hydrosaline volatiles (Ulrich *et al.*, 2001). Daughter mineral compositions show that the brines in the Stillwater Complex were indeed base metal- and sulfur-bearing at the time of their entrapment.

As a consequence of brine–CO_2 immiscibility, volatile exsolution in the Stillwater Complex and other layered intrusions should not be modeled assuming a single-phase fluid. In the Stillwater Complex, two fluids of very different composition may have been present throughout much of the late crystallization history of the intrusion. If the solubilities of ore metals in these phases differ, as has been shown in other magmatic Ni–Cu–PGE sulfide deposits (Hanley *et al.*, 2005), then existing models for the formation of the J-M reef must be revised to consider the presence of two distinct coexisting fluid phases. It is unclear to what extent the volatiles influenced the evolution of the J-M reef, but the potential for (1) interaction of relatively high-temperature, hydrosaline volatiles or low-temperature, metamorphic fluids with grain-boundary hosted sulfide minerals below the J-M reef (Boudreau & Meurer, 1999), (2) modification of the J-M reef ore compositions by hydrosaline fluids and/or late metamorphic fluids, and (3) volatile redistribution of chalcophile metals in other parts of the Stillwater Complex stratigraphy (Meurer *et al.*, 1999) can no longer be dismissed because of the suggested lack of fluid inclusion evidence for high-salinity volatiles.

ACKNOWLEDGEMENTS

NSERC is acknowledged for their financial support to J.J.H. and J.E.M. Dr M. Zientek (US Geological Survey, Spokane) are acknowledged for their assistance in obtaining samples and for providing specific details about the geology of the Stillwater Complex and sample locations that were not available in published form. Earlier versions of the manuscript benefited significantly from discussions with C. Heinrich and M. Gorton, and formal reviews by E. Mathez, A. Boudreau, P. Brown, and R. Frost.

REFERENCES

Arth, J. G. (1976). Behavior of trace elements during magmatic processes; a summary of theoretical models and their applications. *Journal of Research of the US Geological Survey* **4**, 41–47.

Ballhaus, C. G. & Stumpfl, E. F. (1986). Sulphide and platinum mineralization in the Merensky Reef: Evidence from hydrous silicates and fluid inclusions. *Contributions to Mineralogy and Petrology* **94**, 193–204.

Bell, D. R. & Rossman, G. R. (1992). Water in the Earth's mantle: the role of nominally anhydrous minerals. *Science* **255**, 1391–1397.

Bodnar, R. J. (1994). Synthetic fluid inclusions; XII, The system H2O–NaCl; experimental determination of the halite liquidus and isochores for a 40 wt % NaCl solution. *Geochimica et Cosmochimica Acta* **53**, 725–733.

Bonaccorsi, E., Merlino, S., Orlandi, P., Pasero, M. & Vezzalini, G. (1994). Quadridavyne, a new feldspathoid mineral from the Vesuvius area. *European Journal of Mineralogy* **6**, 481–487.

Boudreau, A. E. (1988). Investigations of the Stillwater Complex: IV. The role of volatiles in the petrogenesis of the J-M reef, Minneapolis adit section. *Canadian Mineralogist* **26**, 193–208.

Boudreau, A. E. (1992). Volatile fluid overpressure in layered intrusions and the formation of potholes. *Australian Journal of Earth Sciences* **39**, 277–287.

Boudreau, A. E. (1999). Fluid fluxing of cumulates: the J-M Reef and associated rocks of the Stillwater Complex, Montana. *Journal of Petrology* **40**, 755–772.

Boudreau, A. E. & McCallum, I. S. (1986). Investigations of the Stillwater Complex: III. The Picket Pin Pt/Pd Deposit. *Economic Geology* **81**, 1953–1975.

Boudreau, A. E. & McCallum, I. S. (1992). Concentration of platinum-group elements by magmatic fluids in layered intrusions. *Economic Geology* **87**, 1830–1848.

Boudreau, A. E. & Meurer, W. P. (1999). Chromatographic separation of the platinum-group elements, base metals, gold and sulfur during degassing of a compacting and solidifying igneous crystal pile. *Contributions to Mineralogy and Petrology* **134**, 174–185.

Boudreau, A. E., Mathez, E. A. & McCallum, I. S. (1986). Halogen geochemistry of the Stillwater and Bushveld Complexes: evidence for transport of the platinum-group elements by Cl-rich fluids. *Journal of Petrology* **27**, 967–986.

Boudreau, A. E., Stewart, M. A. & Spivack, A. J. (1997). Stable Cl isotopes and origin of high-Cl magmas. *Geology* **25**, 791–794.

Bowers, T. S. & Helgeson, H. C. (1983). Calculation of the thermodynamic and geochemical consequences of nonideal mixing in the system H_2O–CO_2–NaCl on phase relations in geological systems; equation of state for H_2O–CO_2–NaCl fluids at high pressures and temperatures. *Geochimica et Cosmochimica Acta* **47**, 1247–1275.

Brantley, S. L. & Voigt, D. (1989). Fluids in metamorphic rocks; effects of fluid chemistry on quartz microcrack healing. In: Fritz, P. & Frape, S.K. (eds). *Proceedings of the International Symposium on Water–Rock Interaction* St. John's, Newfoundland, Canada: Geological Association of Canada. **6**, 113–116.

Braun, K., Meurer, W., Boudreau, A. E. & McCallum, I. S. (1994). Compositions of pegmatoids beneath the J-M Reef of the Stillwater Complex, Montana, U.S.A. *Chemical Geology* **113**, 245–257.

Bray, C. J. & Spooner, E. T. C. (1992). Fluid inclusion volatile analysis by gas chromatography with photoionization/micro-thermal conductivity detectors; applications to magmatic MoS2 and other H_2O–CO_2 and H_2O–CH_4 fluids. *Geochimica et Cosmochimica Acta* **56**, 261–272.

Bromiley, G. D. & Keppler, H. (2004). An experimental investigation of hydroxyl solubility in jadeite and Na-rich clinopyroxenes. *Contributions to Mineralogy and Petrology* **147**, 189–200.

Campbell, I. H., Naldrett, A. J. & Barnes, S. J. (1983). A model for the origin of the platinum-rich sulfide horizons in the Bushveld and Stillwater Complexes. *Journal of Petrology* **24**, 33–165.

Cawthorn, R. G. (1999). Geological models for platinum-group metal mineralization in the Bushveld Complex. *South African Journal of Science* **95**, 490–498.

Cesare, B. (1995). Graphite precipitation within C–O–H fluid inclusions: closed-system chemical and density changes, and thermobarometric implications. *Contributions to Mineralogy and Petrology* **122**, 25–33.

Czamanske, G. K. & Loferski, P. J. (1996). Cryptic trace-element alteration of anorthosite, Stillwater Complex, Montana. *Canadian Mineralogist* **34**, 559–576.

Czamanske, G. K., Zientek, M. L. & Manning, C. E. (1991). Low-K granophyres of the Stillwater Complex, Montana. *American Mineralogist* **76**, 1646–1661.

De Vivo, B., Torok, K., Ayuso, R. A., Lima, A. & Liren, L. (1995). Fluid inclusion evidence for magmatic silicate/saline/CO_2 immiscibility and geochemistry of alkaline xenoliths from Ventotene Island, Italy. *Geochimica et Cosmochimica Acta* **59**, 2941–2953.

DePaolo, D. J. & Wasserburg, G. J. (1979). Sm–Nd age of the Stillwater Complex and the mantle evolution curve for neodymium. *Geochimica et Cosmochimica Acta* **43**, 999–1008.

Duan, Z., Moller, N. & Weare, J. H. (1995). Equation of state for the NaCl–H_2O–CO_2 system: Prediction of the phase equilibria and volumetric properties. *Geochimica et Cosmochimica Acta* **59**, 2869–2882.

Erwood, R. J., Kesler, S. E. & Cloke, P. L. (1979). Compositionally-distinct, saline hydrothermal solutions, Naica Mine, Chihuahua, Mexico. *Economic Geology* **74**, 95–108.

Frantz, J. D., Popp, R. K. & Hoering, T. C. (1992). The compositional limits of fluid immiscibility in the system H_2O–NaCl–CO_2 as determined with the use of synthetic fluid inclusions in conjunction with mass spectrometry. *Chemical Geology* **98**, 237–255.

Frezzotti, M. L., Burk, E. A. J., DeVivo, B., Stefanini, B. & Villa, I. M. (1992). Mantle fluids in pyroxenite nodules from Salt Lake Crater (Oahu, Hawaii). *European Journal of Mineralogy* **4**, 1137–1153.

Frost, B. R. & Touret, J. L. R. (1989). Magmatic CO2 and saline melts from the Sybille monzosyenite, Laramie anorthosite complex, Wyoming. *Contributions to Mineralogy and Petrology* **103**, 178–186.

Fujimaki, H., Tatsumoto, M. & Aoki, K.-I. (1984). Partition coefficients of Hf, Zr and REE between phenocrysts and groundmass. *Journal of Geophysical Research* **B-89**, 662–672.

Glebovitsky, V. A., Semenov, V. S., Belyatsky, B.V., Koptev-Dvornikov, E. V., Pchelintseva, N. F., Kireev, B. S. & Koltsov, A. B. (2001). The structure of the Lukkulaisvaara Intrusion, Oulanka Group, Northern Karelia: Petrological Implications. *Canadian Mineralogist* **39**, 607–637.

Goldstein, R. H. (2003). Petrographic analysis of fluid inclusions. In: Samson, I., Marshall, D. & Anderson, A. (eds) *Fluid Inclusions: analysis and Interpretation. Mineralogical Association of Canada, Short Course Series* **32**, 9–54.

Hanley, J. J., Mungall, J. E., Pettke, T., Spooner, E. T. C. & Bray, C. J. (2005). Ore metal redistribution by hydrocarbon–brine and hydrocarbon–halide melt phases, North Range footwall of the Sudbury Igneous Complex, Ontario, Canada. *Mineralium Deposita* **40**, 237–256.

Helz, R. T. (1985). Compositions of fine-grained mafic rocks from sills and dykes associated with the Stillwater Complex. In: Czamanske, G. K. & Zientek, M. L. (eds) *The Stillwater Complex, Montana: Geology and Guide. Montana Bureau of Mines and Geology, Special Publication* **92**, 97–117.

Heyen, G., Ramboz, C. & Dubessy, J. (1982). Simulation of phase equilibria in the system CO_2–CH_4 at 50°C and 100 bar: application to fluid inclusions. *Comptes Rendus de l'Académie des Sciences, Série 2* **294**, 203–206.

Heyse, J. V. (1983). The mineralogy of the Stillwater platinum–palladium ore in the Frog Pond and Minneapolis adits. Internal Report, Chevron Research Company, San Ramon, California, USA.

Holland, T. & Blundy, J. (1994). Non-ideal interactions in calcic amphiboles and their bearing on amphibole–plagioclase thermometry. *Contributions to Mineralogy and Petrology* **116**, 433–447.

Holtz, F., Pichavant, M., Barbey, P. & Johannes, W. (1992). Effects of H2O on liquidus phase relations in the haplogranite system at 2 and 5 kbar. *American Mineralogist* **77**, 1223–1241.

Jenkins, D. M. & Chernosky, J. V. (1986). Phase equilibria and crystallographic properties of Mg-chlorite. *American Mineralogist* **71**, 924–936.

Joyce, D. B. & Holloway, J. R. (1993). An experimental determination of the thermodynamic properties of H_2O–CO_2–NaCl fluids at high pressures and temperatures. *Geochimica et Cosmochimica Acta* **57**, 733–746.

Kamenetsky, V. S., Naumov, V. B., Davidson, P., van Achterbergh, E. & Ryan, C. G. (2004*a*). Immiscibility between silicate magmas and aqueous fluids: a melt inclusion pursuit into the magmatic–hydrothermal transition in the Omsukchan Granite (NE Russia). *Chemical Geology* **210**, 73–90.

Kamenetsky, M. B., Sobolev, A. V. & Kamenetsky, V. S. (2004*b*). Kimberlite melts rich in alkali chlorides and carbonates: A potent metasomatic agent in the mantle. *Geology* **32**, 845–848.

Klemme, S. (2004). Evidence for fluoride melts in Earth's mantle formed by liquid immiscibility. *Geology* **32**, 441–444.

Labotka, T. C. (1985). Petrogenesis of metamorphic rocks beneath the Stillwater Complex: Assemblages and conditions of metamorphism. In: Czamanske, G. K. & Zientek, M. L. (eds) *The Stillwater Complex, Montana: Geology and Guide. Montana Bureau of Mines and Geology, Special Publication* **92**, 70–76.

Labotka, T. C. & Kath, R. L. (2001). Petrogenesis of the contact-metamorphic rocks beneath the Stillwater Complex, Montana. *Geological Society of America Bulletin* **113**, 1312–1232.

Larsen, R. B., Brooks, C. K. & Bird, D. K. (1992). Methane-bearing, aqueous, saline solutions in the Skaergaard intrusion, east Greenland. *Contributions to Mineralogy and Petrology* **112**, 428–437.

Lechler, P. J., Arehart, G. B. & Knight, M. (2002). Multielement and isotopic geochemistry of the J-M Reef, Stillwater Intrusion, Montana. In: Boudreau, A (ed.) *Proceedings of the Ninth International Platinum Symposium*, 245–248.

Lowenstern, J. B. (1994). Chlorine, fluid immiscibility, and degassing in peralkaline magmas from Pantelleria, Italy. *American Mineralogist* **79**, 353–369.

Marcantonio, R., Zindler, A., Reisberg, L. & Mathez, E. A. (1993). Re–Os isotopic systematics in chromitites from the Stillwater Complex, Montana, U.S.A. *Geochimica et Cosmochimica Acta* **57**, 4029–4037.

Mathez, E. A. & Webster, J. D. (2005). Partitioning behavior of chlorine and fluorine in the system apatite–silicate melt–fluid. *Geochimica et Cosmochimica Acta* **69**, 1275–1286.

Mathez, E. A., Dietrich, V. J., Holloway, J. R. & Boudreau, A. E. (1989). Carbon distribution in the Stillwater Complex and evolution of vapor during crystallization of Stillwater and Bushveld magmas. *Journal of Petrology* **30**, 153–173.

Mavrogenes, J. A. & Bodnar, R. J. (1994). Hydrogen movement into and out of fluid inclusions in quartz; experimental evidence and geological implications. *Geochimica et Cosmochimica Acta* **58**, 141–148.

McBirney, A. R. (2002). The Skaergaard layered series: Part VI, excluded trace elements. *Journal of Petrology* **43**, 535–556.

McCallum, I. S., Raedeke, L. D. & Mathez, E. A. (1980). Investigations of the Stillwater Complex: I. Stratigraphy and structure of the banded zone. *American Journal of Science* **280A**, 59–87.

McCallum, I. S., Thurber, M. W., O'Brien, H. E. & Nelson, B. K. (1999). Lead isotopes in sulfides from the Stillwater Complex, Montana: evidence for subsolidus remobilization. *Contributions to Mineralogy and Petrology* **137**, 206–219.

McDonough, W. A. & Sun, S. S. (1995). The composition of the Earth. *Chemical Geology* **120**, 223–253.

Merlino, S., Bonaccorsi, E. & Pasero, M. (1992). New minerals in the cancrinite group: crystal chemistry and phase transformations. *International Geological Congress, Abstracts* **29**, 672.

Meurer, W. P. & Boudreau, A. E. (1998). Compaction of igneous cumulates: Part I, Geochemical consequences for cumulates and liquid fractionation trends. *Journal of Geology* **106**, 281–292.

Meurer, W. P., Klaber, S. & Boudreau, A. E. (1997). Discordant bodies from olivine-bearing zones III and IV of the Stillwater Complex, Montana—evidence for postcumulus fluid migration and reaction in layered intrusions. *Contributions to Mineralogy and Petrology* **130**, 81–92.

Meurer, W. P., Willmore, C. C. & Boudreau, A. E. (1999). Metal redistribution during fluid exsolution and migration in the Middle Banded series of the Stillwater Complex, Montana. *Lithos* **47**, 143–156.

Mungall, J. E. (2002). Kinetic controls on the partitioning of trace elements between silicate and sulphide liquids. *Journal of Petrology* **43**, 749–768.

Murck, B. W., Burruss, R. C. & Hollister, L. S. (1978). Phase equilibria in fluid inclusions in ultramafic xenoliths. *American Mineralogist* **63**, 40–46.

Newton, R. C. & Manning, C. E. (2000). Quartz solubility in H2O–NaCl and H_2O–CO_2 solutions at deep crust–upper mantle pressures and temperatures: 2–15 kbar and 500–900°C. *Geochimica et Cosmochimica Acta* **64**, 2993–3005.

Newton, R. C. & Manning, C. E. (2002). Experimental determination of calcite solubility in H_2O–NaCl solutions at deep crust/upper mantle pressures and temperatures: Implications for metasomatic processes in shear zones. *American Mineralogist* **87**, 1401–1409.

Newton, R. C., Aranovich, L. Ya., Hansen, E. C. & Vandenheuvel, B. A. (1998). Hypersaline fluids in Precambrian deep-crustal metamorphism. *Precambrian Research* **91**, 41–63.

Nunes, P. D. & Tilton, G. R. (1971). Uranium–lead ages of minerals from the Stillwater Complex and associated rocks, Montana. *Geological Society of America Bulletin* **82**, 2231–2250.

Ohmoto, H. & Kerrich, D. (1977). Devolatilization equilibria in graphitic systems. *American Journal of Science* **277**, 1013–1044.

Page, N. J. (1976). Serpentinization and alteration in an olivine cumulate from the Stillwater Complex, southwestern Montana. *Contributions to Mineralogy and Petrology* **54**, 127–137.

Page, N. J. (1977). *Stillwater Complex, Montana: rock succession, metamorphism, and structure of the complex and adjacent rocks. US Geological Survey Professional Paper* **999**.

Page, N.J. & Nokleberg, W.J. (1974). *Geologic map of the Stillwater Complex*, Montana: U.S. Geological Survey Map I-797, 5 sheets, scale 1:12,000.

Polovina, J. S., Hudson, D. M. & Jones, R. E. (2004). Petrographic and geochemical characteristics of postmagmatic hydrothermal alteration and mineralization in the J-M Reef, Stillwater Complex, Montana. *Canadian Mineralogist* **42**, 261–278.

Renno, A. D., Leander, F., Witzke, T. & Herzig, P. M. (2004). The coexistence of melts of hydrous copper chloride, sulfide and silicate compositions in a magnesiohastingsite cumulate, TUBAF seamount, Papua New Guinea. *Canadian Mineralogist* **42**, 1–16.

Richard, L. R. (1995). *MinPet: Mineralogical and petrological data processing system, version 2.02*. Québec: MinPet Geological Software.

Ripley, E. M. (2005). Re/Os isotopic and fluid inclusion studies of fluid–rock interaction in the contact aureole of the Duluth Complex, Minnesota. *Geochimica et Cosmochimica Acta* **69**, 10, Supplemental 332.

Roedder, E. (1984). Fluid inclusions. In: Ribbe, P. H. (ed.) *Mineralogical Society of America. Reviews in Mineralogy* **12**.

Roedder, E. & Bodnar, R. J. (1980). Geological pressure determinations from fluid inclusion studies. *Annual Review of Earth and Planetary Sciences* **8**, 263–301.

Roedder, E. & Coombs, D. S. (1967). Immiscibility in granitic melts, indicated by fluid inclusions in ejected granitic blocks from Ascension island. *Journal of Petrology* **8**, 417–449.

Saxena, S. K. & Fei, Y. (1988). Fluid mixtures in the C–H–O system at high pressure and temperature. *Geochimica et Cosmochimica Acta* **52**, 505–572.

Schiffries, C. M. (1982). The platiferous dunite pipe in the Bushveld complex: infiltration metasomatism by a chloride solution. *Economic Geology* **77**, 1439–1453.

Schiffries, C. M. (1990). Liquid absent aqueous fluid inclusions and phase equilibria in the system $CaCl_2$–NaCl–H_2O. *Geochimica et Cosmochimica Acta* **54**, 611–619.

Schiffries, C. M. & Skinner, B. J. (1987). The Bushveld hydrothermal system: field and petrologic evidence. *American Journal of Science* **287**, 566–595.

Shepherd, T. J., Rankin, A. H. & Alderton, D. H. M. (1985). *A Practical Guide to Fluid Inclusions*. Glasgow: Blackie.

Shinohara, H. (1994). Exsolution of immiscible vapor and liquid phases from a crystallizing silicate melt: Implications for chlorine and metal transport. *Geochimica et Cosmochimica Acta* **58**, 5215–5221.

Shinohara, H., Iiyama, T. J. & Matsuo, S. (1989). Partition of chlorine compounds between silicate melt and hydrothermal solutions: I, Partition of NaCl–KCl. *Geochimica et Cosmochimica Acta* **53**, 2617–2630.

Sonnenthal, E. L. (1992). Geochemistry of dendritic anorthosites and associated pegmatites in the Skaergaard Intrusion, East Greenland: Evidence for metasomatism by a chlorine-rich fluid. *Journal of Volcanology and Geothermal Research* **52**, 209–230.

Sourirajan, S. & Kennedy, G. C. (1962). The system H_2O–NaCl at elevated temperatures and pressures. *American Journal of Science* **260**, 115–141.

Sterner, S. M., Hall, D. L. & Bodnar, R. J. (1988). Synthetic fluid inclusions: V, Solubility relations in the system NaCl–KCl–H_2O under vapor-saturated conditions. *Geochimica et Cosmochimica Acta* **52**, 989–1005.

Stumpfl, E. F. (1974). The genesis of platinum deposits: further thoughts. *Minerals Science Engineering* **6**, 120–141.

Stumpfl, E. F. & Rucklidge, J. C. (1982). The platiniferous dunite pipes of the eastern Bushveld Complex. *Economic Geology* **77**, 1419–1431.

Tullis, J. (2001). Effects of deformation on fluid distribution in aggregates. *Geological Society of America, Abstracts with Programs* **33**, 50.

Ulrich, T., Gunther, D. & Heinrich, C. A. (2001). The evolution of a porphyry Cu–Au deposit, based on LA-ICP-MS analysis of fluid inclusions; Bajo de la Alumbrera, Argentina. *Economic Geology* **96**, 1743–1774.

van den Kerkhof, A. M. & Olsen, S. N. (1990). A natural example of superdense CO2 inclusions: microthermometry and Raman analysis. *Geochimica et Cosmochimica Acta* **54**, 895–901.

Volborth, A. A. & Housley, R. M. (1984). A preliminary description of complex graphite, sulfide, arsenide, and platinum group element mineralization in a pegmatoid pyroxenite of the Stillwater Complex, Montana, U.S.A. *Tschermaks Mineralogische und Petrographische Mitteilungen* **33**, 213–230.

Volborth, A. A., Tarkian, M., Stumpfl, E. F. & Housley, R. M. (1986). A survey of the Pd–Pt mineralization along the 35 km strike of the J-M reef, Stillwater Complex, Montana. *Canadian Mineralogist* **24**, 459–481.

Webster, J. D. (1997). Exsolution of Cl-bearing fluids from chlorine-enriched mineralizing granitic magmas and implications for ore metal transport. *Geochimica et Cosmochimica Acta* **61**, 1017–1030.

Webster, J. D. (2004). The exsolution of magmatic hydrosaline chloride liquids. *Chemical Geology* **210**, 33–48.

Webster, J. D., Kinzler, R. J. & Mathez, E. A. (1999). Chloride and water solubility in basalt and andesite melts and implications for magmatic degassing. *Geochimica et Cosmochimica Acta* **63**, 729–738.

Williams, T. J., Candela, P. A. & Piccoli, P. M. (1995). The partitioning of copper between silicate melts and two-phase aqueous fluids: an experimental investigation at 1 kbar, 800°C, and 0·5 kbar, 850°C. *Contributions to Mineralogy and Petrology* **121**, 388–399.

Williams-Jones, A. E. & Samson, I. M. (1990). Theoretical estimation of halite solubility in the system NaCl–$CaCl_2$–H_2O: applications to fluid inclusions. *Canadian Mineralogist* **28**, 299–304.

Willmore, C. C., Boudreau, A. E. & Kruger, F. J. (2000). The halogen geochemistry of the Bushveld Complex, Republic of South Africa: Implications for chalcophile element distribution in the Lower and Critical zones. *Journal of Petrology* **41**, 1517–1539.

Yardley, B. W. D. (1989). *An Introduction to Metamorphic Petrology*. Harlow: Longman.

Zhang, Y. G. & Frantz, J. D. (1987). Determination of the homogenization temperatures and densities of supercritical fluids in the system NaCl–KCl–$CaCl_2$–H_2O using synthetic fluid inclusions. *Chemical Geology* **64**, 335–350.

Zientek, M. L., Cooper, R. W., Corson, S. R. & Geraghty, E. P. (2002). Platinum-group element mineralization in the Stillwater Complex. In: Cabri, L. (ed.) *The Geology, Geochemistry, Mineralogy and Mineral Beneficiation of Platinum-Group Elements. Canadian Institute of Mining, Metallurgy and Petroleum, Special Volume* **54**, 459–481.